Monthly Notices of the ROYAL ASTRONOMICAL SOCIETY

MNRAS **515,** 1580–1597 (2022) https://doi.org/10.1093/mnras/stac1804
Advance Access publication 2022 July 4

Antenna beam characterization for the global 21-cm experiment LEDA and its impact on signal model parameter reconstruction

M. Spinelli [1,2,3]★ G. Kyriakou,[4,5]★ G. Bernardi,[6,7,8] P. Bolli,[4] L. J. Greenhill,[9] A. Fialkov[10,11] and H. Garsden[9,12]

[1]*Institute for Particle Physics and Astrophysics, ETH Zürich, Wolfgang Pauli Strasse 27, CH-8093 Zürich, Switzerland*
[2]*Department of Physics and Astronomy, University of the Western Cape, Robert Sobukhwe Road, Bellville 7535, South Africa*
[3]*INAF-Osservatorio Astronomico di Trieste, Via G.B. Tiepolo 11, I-34143 Trieste, Italy*
[4]*INAF-Osservatorio Astronomico di Arcetri, Largo Enrico Fermi 5, I-50125 Firenze, Italy*
[5]*Department of Physics and Astronomy, University of Florence, P.za di San Marco, 4, I-50121 Firenze, Italy*
[6]*INAF-Istituto di Radioastronomia, via Gobetti 101, I-40129 Bologna, Italy*
[7]*Department of Physics & Electronics, Artillery Road, Rhodes University, 6139 Makhanda, South Africa*
[8]*South African Radio Astronomy Observatory, 2 Fir street, Observatory, 7925 Cape Town, South Africa*
[9]*Center for Astrophysics, Harvard & Smithsonian, 60 Garden Street, Cambridge MA 02138, USA*
[10]*Kavli Institute for Cosmology, University of Cambridge, Madingley Road, Cambridge CB3 0HA, UK*
[11]*Institute of Astronomy, University of Cambridge, Madingley Road, Cambridge CB3 0HA, UK*
[12]*Astronomy Unit, School of Physical and Chemical Sciences, Queen Mary University of London, Mile End Road, London, E1 4NS, UK*

Accepted 2022 June 22. Received 2022 June 16; in original form 2022 April 19

ABSTRACT

Cosmic dawn, the onset of star formation in the early universe, can in principle be studied via the 21-cm transition of neutral hydrogen, for which a sky-averaged absorption signal, redshifted to MHz frequencies, is predicted to be $O(10–100)$ mK. Detection requires separation of the 21-cm signal from bright chromatic foreground emission due to Galactic structure, and the characterization of how it couples to instrumental response. In this work, we present characterization of antenna gain patterns for the Large-aperture Experiment to detect the Dark Ages (LEDA) via simulations, assessing the effects of the antenna ground-plane geometries used, and measured soil properties. We then investigate the impact of beam pattern uncertainties on the reconstruction of a Gaussian absorption feature. Assuming the pattern is known and correcting for the chromaticity of the instrument, the foregrounds can be modelled with a log-polynomial, and the 21-cm signal identified with high accuracy. However, uncertainties on the soil properties lead to percentage changes in the chromaticity that can bias the signal recovery. The bias can be up to a factor of two in amplitude and up to few per cent in the frequency location. These effects do not appear to be mitigated by larger ground planes, conversely gain patterns with larger ground planes exhibit more complex frequency structure, significantly compromising the parameter reconstruction. Our results, consistent with findings from other antenna design studies, emphasize the importance of chromatic response and suggest caution in assuming log-polynomial foreground models in global signal experiments.

Key words: instrumentation: miscellaneous – dark ages, reionization, first stars.

1 INTRODUCTION

The 21-cm transition of neutral hydrogen (HI) is predicted to trace cold diffuse gas during cosmic dawn, the epoch during which the first generation of stars formed, ∼100 Myr after the big bang. Prior to this, the spin temperature of the transition was likely in equilibrium with the cosmic microwave background, well above the gas kinetic temperature. The rise of Ly-α background radiation from pockets of star formation coupled the spin temperature to the gas kinetic temperature via the Wouthuysen–Field effect (WF, Wouthuysen 1952; Field 1958). The growing population of stellar remnants created an X-ray background that drove the gas kinetic and the spin temperatures higher (e.g. Furlanetto, Oh & Briggs 2006; Pritchard & Loeb 2010). Averaged over the sky, the relative proportion of Ly-α coupling and X-ray heating varied with redshift and could create a broad absorption trough in the spectrum of the cosmic microwave background.

Detection of the predicted trough would provide unique information about the formation of the first luminous structures in the Universe (e.g. Barkana & Loeb 2005; Furlanetto et al. 2006; Fialkov et al. 2013; Mirocha 2014; Mesinger, Greig & Sobacchi 2016; Mirocha & Furlanetto 2019; Reis, Fialkov & Barkana 2020; Magg et al. 2021; Gessey-Jones et al. 2022; Reis, Barkana & Fialkov 2022), and of the thermal history of the intergalactic medium (Pritchard & Furlanetto 2007; Mesinger, Ferrara & Spiegel 2013; Fialkov, Barkana & Visbal 2014; Reis, Fialkov & Barkana 2021).

The signal redshifted to radio frequencies $\lesssim$100 MHz and of order −100 mK in amplitude would in principle be detectable using meter-scale antennas and an integration time on the order of 100 h, for sufficiently accurate radiometric calibration, and well understood

★ E-mail: mspinelli@phys.ethz.ch (MS); georgios.kyriakou@inaf.it (GK)

celestial foregrounds (1000–10 000 K) and antenna gain patterns as a function of frequency.

The scientific importance of a measurement of the 21-cm global signal absorption feature has motivated the effort to build several experiments in different locations and with different technical approaches.

The experiment to detect the global epoch-of-reionization signature (EDGES) relies upon a broad-band horizontal 'blade' dipole design and is deployed at the Murchison radio-astronomy observatory (MRO) in western Australia. It reported the detection of a broad −520 mK absorption profile centred at ∼78 MHz (Bowman et al. 2018) supported by validation tests also described by Mahesh et al. (2021). The profile, more than a factor two deeper than predicted from theory based on standard physics (e.g. Cohen et al. 2017; Reis et al. 2021), has triggered several studies aimed at an understanding of its origin. From a theoretical point of view, such a result could imply that either the temperature of the radio background is higher than the CMB (e.g. Bowman et al. 2018; Feng & Holder 2018; Reis et al. 2020) or the neutral gas at redshift ∼17 was colder than expected, possibly due to the interaction with dark matter (e.g. Barkana 2018; Muñoz & Loeb 2018; Fialkov & Barkana 2019; Liu et al. 2019). Other studies suggested the presence of un-modelled systematics (Hills et al. 2018; Singh & Subrahmanyan 2019; Spinelli, Bernardi & Santos 2019; Bevins et al. 2020), weaknesses in the analysis pipeline due to inaccurate modelling of the foregrounds (e.g. Singh & Subrahmanyan 2019), along with flaws in the statistical interpretation of the data (e.g. Sims & Pober 2020).

The third generation of the Shaped Antenna measurement of the background RAdio Spectrum (SARAS) features a spectral radiometer based on a monocone antenna and receiver floated on a lake in southern India (Jishnu Nambissan et al. 2021), has recently presented an analysis of their data (Singh et al. 2021), rejecting the EDGES absorption profile at 95.3 per cent confidence level.

Besides EDGES and SARAS, there are several 21-cm global signal experiments underway, such as the probing radio intensity at high-Z from Marion (PRIZM) experiment (Philip et al. 2019), the Broad-band Instrument for Global HydrOgen ReioNization Signal (BIGHORNS; Sokolowski et al. 2015), the radio experiment for the analysis of cosmic hydrogen (REACH) (Cumner et al. 2022) and the Mapper of the IGM spin temperature (MIST).[1]

This work focuses on the large-aperture experiment to detect the dark age (LEDA; Price et al. 2018) equipped and operated between two and five dual polarization antennas within the Owens valley radio observatory long wavelength array station (OVRO-LWA) for radiometry, using custom RF and digital signal processing to enable the requisite timing, calibration, and stability (2013–2020).

Using early radiometric data, Bernardi et al. (2016) set a coarse upper limit for the amplitude and the width for the anticipated absorption trough. Using later data (December 2018–May 2019), Spinelli et al. (2021) constrained the spectral index, β, of Galactic radio emission in the northern sky (60–87 MHz), obtaining values compatible with expectation from simulations and other measurements. We note that study by Garsden et al. (2021) was distinct, using contemporaneous interferometric data, generated by the LEDA correlator that was part of OVRO-LWA, to characterize the effect of systematic errors in calibration on dynamic range for 2D cylindrical spatial power spectra. (See also Eastwood et al. (2018) regarding an alternate approach, also using LEDA interferometric data.)

[1] http://www.physics.mcgill.ca/mist/

The critical challenge in analysing radiometric data is accurate subtraction of the bright foregrounds, normally attempted by modelling the spectrally smooth emission with an N-term log-polynomial and performing Bayesian inference for both foreground and background signals (e.g. Bernardi, McQuinn & Greenhill 2015; Bernardi et al. 2016; Bowman et al. 2018; Singh et al. 2021).

Chromaticity is a key factor in antenna design (e.g. Mozdzen et al. 2016; Jishnu Nambissan et al. 2021; Cumner et al. 2022) and chromatic beam effects can limit the effectiveness of foreground subtraction (e.g. Vedantham et al. 2014). Accurate antenna beam simulations, including realistic ground plane and soil descriptions, are thus fundamental to understand radiometric data. Mahesh et al. (2021) explored antenna beam modelling as a source of uncertainty in global signal measurement, checking the stability of the signal reported by EDGES with respect to choice of numerical electromagnetic solver code. Bradley et al. (2019) instead investigated how a possible systematic artefact within the antenna ground plane may produce broad absorption features in the spectra.

In preparation for future data analysis, the REACH project has developed a software pipeline that can incorporate more efficiently, the effect of beam chromaticity coupled with a non-trivial scaling in frequency of the foreground (Anstey, de Lera Acedo & Handley 2020). This strategy, although computationally costly, leads to robust 21-cm global signal extraction in simulations and can thus enable better informed optimization of antenna design (Anstey et al. 2022; Cumner et al. 2022). Other techniques that incorporate beam effects in the foreground model using machine learning methods have been proposed by Tauscher, Rapetti & Burns (e.g. 2020); Tauscher et al. (e.g. 2021).

In this paper, we make use of the common log-polynomial model to parametrize LEDA mock simulated spectra and we analyse in detail its limitations when a refined soil modelling with realistic values of its dielectric properties and conductivity is considered. We explore different ground planes, focusing on the ones used in the field during data acquisition and discuss the impact on the Bayesian reconstruction of signal and foreground parameters.

This paper is organized as follows. We describe *in situ* measurements of soil complex-permittivity and improved electromagnetic simulations in Section 2, including the details of the multi-layer modelling of the ground. We describe the construction of simulated spectra in Section 3.1 and the computation of the chromaticity correction factor in Section 3.2. In Section 3.3, we discuss the accuracy of the smooth foreground approximation in the presence of realistic beam modelling. We analyse in Section 4, the impact of our realistic beam on the reconstruction of the parameters describing a neutral hydrogen absorption feature. A discussion of the results and our conclusions are presented in Section 5.

2 MODELLING LEDA ANTENNAS

In this section we present in detail improved electromagnetic models for antennas used for radiometry by LEDA. Driven by science requirements, the frequency range of interest is between 50 and 87 MHz (although some of the simulation results are shown in a larger frequency range). In Section 2.1, we present the antenna geometry and the ground planes we have considered. Note that the models reflect as built designs. In Section 2.2, we describe the *in situ* soil permittivty data gathering. In Section 2.3, we review the analytic beam model used in previous analyses of LEDA data, while the focus of Section 2.4 is incorporation of the soil permittivty data and alternate ground-plane geometries.

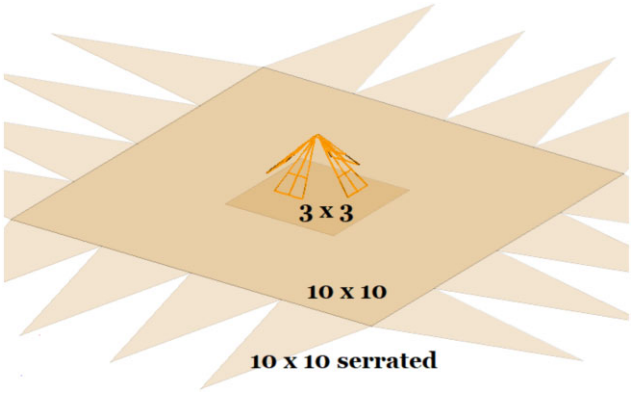

Figure 1. LEDA antenna 3D view of geometry with the ground planes to be used in the analysis. Dimensions are shown in meters.

2.1 Antenna and ground plane description

We outline here the basic geometrical properties of the antennas used by LEDA for radiometry, which excluding the ground plane are similar to those used in general for construction of long wavelength array stations (Taylor et al. 2012, and references therein) and OVRO-LWA specifically.

Each antenna comprises two pairs of triangular dipole arms 1.50 m long, angled downward by 45° (Fig. 1). We focus our analysis on the east–west orientation.

The default OVRO-LWA antenna ground plane (Paravastu et al. 2007; Schmitt et al. 2009) is a 3 × 3 m galvanized welded steel mesh with 2.51 mm wire diameter (12.5 gauge) and 10.2 cm spacing. In this analysis, we modelled the beam for one antenna, numbered 252 (Price et al. 2018), with three ground plane configurations that corresponded to a series of test modifications made in the field (Spinelli et al. 2021). The 3 × 3 m ground plane was replaced first by a 10 × 10 m patch of mesh comprising the same material but with a 3.06 mm wire diameter (11 gauge), and later by the same but with serrations as represented by four 5 m long, 1.25 m wide isosceles triangles positioned on each side (referred to as the serrated ground plane). The arrangement is shown schematically in Fig. 1. As in Bowman et al. (2018), peripheral serrations are sometimes added to ground planes to reduce coherence among currents proximate to the edge discontinuity.

2.2 Characterization of soil complex permittivity

Measurements of complex permittivity, using coaxial impedance dielectric reflectometry (Seyfried & Murdock 2004), were made at three depths (4, 14, and, 21 ± 0.5 inches, corresponding to 10.16, 35.56, and 53.34 cm) in a test pit dug at a midpoint ∼170 m from antennas 252, 254, and backfilled. Three 50 MHz sensors were inserted into the undisturbed strata revealed along one wall of the pit. Sensor firmware provided temperature-corrected estimates of permittivity using the US department of agriculture calibration for soil comprising sand, silt, and clay with conductivity $<1.5\,\mathrm{S\,m^{-1}}$ (Seyfried et al. 2005).

Data were collected episodically from May 2019 to January 2020, at epochs spaced in time so as to track complex permittivity during the precipitation-free summer and fall seasons, as it approached baseline values. Scatter in conductivity measurements was $0.001\,\mathrm{S\,m^{-1}}$ and ≤0.02 in the real part of permittivity.

The soil composition observed at the test pit above 53 cm depth was similar to that removed from a 1.5 m deep vertical auger hole drilled ∼10 m SE of antenna 252: sand and a mix of sand and pebbles (<5 mm), depending on depth. These observations are consistent with the broader geological context of this part of the Owens valley. Tallyn (2002) classify the soil deposits on level terrain near the steep front of the Inyo range to the east as deep, well-drained Mazourka-Cajon-Hessica formations of sandy soil. With finer positional resolution, Danskin (1998) describe well-sorted and unconsolidated lacustrine deposits of sand, gravelly sand, and, silty sand to depths on the order of 100 m in the vicinity of the Black mountain, which overlooks the site from the ENE. This layering and favourable drainage across a broad area, and the absence of bedrock, buried boulders, and volcanic debris suggest that even without the benefit of ground penetrating radar analyses, it is reasonable to anticipate that the antenna sites are likely to be good ones from a geological perspective.

2.3 Analytic beam model

We summarize in this section, the analytical beam model of the LWA dipole used in previous works. For a more extensive description see Dowell (2011), Taylor et al. (2012), Ellingson et al. (2013). Previous LEDA studies (Bernardi et al. 2015; Spinelli et al. 2019) used this beam modelling. This model allows the reconstruction of the antenna beam pattern in every azimuth direction, using two principle antenna planes (E and H, effectively taking into account the antenna symmetries) and reads:

$$A(\theta, \phi, \nu) = \sqrt{[p_E(\theta, \nu)\cos\phi]^2 + [p_H(\theta, \nu)\sin\phi]^2}.$$

The pattern in the E- and H-plane is given by:

$$p_i(\nu, \theta) = \left[1 - \left(\frac{\theta}{\pi/2}\right)^{\alpha_i(\nu)}\right](\cos\theta)^{\beta_i(\nu)} + \gamma_i(\nu)\left(\frac{\theta}{\pi/2}\right)(\cos\theta)^{\delta_i(\nu)} \quad (1)$$

where $i = E, H$, and θ is the elevation angle. The behaviour of the coefficients $[\alpha_i, \beta_i, \gamma_i, \delta_i]$ with respect to frequency is fitted with a polynomial of n^{th}-order[2] to NEC4 simulations (Hicks et al. 2012). Note that for this simulation only the 3 × 3 ground plane case is available.

2.4 Improving the beam model

In this section, we incorporate the soil properties measured *in situ*, describing more realistically the environmental conditions in which the data have been collected. Although not previously explored for the LEDA antennas, there are examples in the literature of similar studies where the soil is analysed as an homogeneous dielectric semi-infinite volume, discriminating only between dry and wet soil conditions (e.g. Sutinjo et al. 2015), or a combination of both, as in Bradley et al. (2019).

2.4.1 One layer baseline model

For our new simulation we use FEKO,[3] a commercial software widely employed in numerical EM simulations and based on the method of moments (MoM, e.g. Davidson (2010)).

[2]Different works throughout the years have use different value for the polynomial order. Bernardi et al. (2016), Spinelli et al. (2019) used a 3rd order polynomial while Spinelli et al. (2021) used a 13th order polynomial.
[3]https://altairhyperworks.com/feko/

Table 1. Soil parameters for the one-layer and the multi-layer model extracted from measurements of soil at the LWA site during both dry and wet conditions at depths z_i, $i = 1, 2, 3$.

Soil layer parameters (σ in S/m, ϵ_r dimensionless)				
	$\sigma_{\rm dry}$	$\sigma_{\rm wet}$	$\epsilon_{r,\rm dry}$	$\epsilon_{r,\rm wet}$
one layer	0.004	0.01	4.4	6.5
$z_1 = 10.16$ cm	0.0013	0.005	3.73	8.09
$z_2 = 35.56$ cm	0.004	0.0068	4.25	6.45
$z_3 = 53.34$ cm	0.0187	0.0388	7.58	20.56

Table 2. Number of soil layers that were used in each of our three multi-layer models: $\lambda_p/10$ is for the first iteration of the algorithm, and converged is the final step of doubling that allows gain convergence to 0.1 dB.

	Number of soil layers for multi-layer schemes		
	Measurements	$\lambda_p/10$	Converged
dry	3	5	40
wet	3	7	56

We model the soil as a single half-infinite layer of constant complex permittivity and conductivity, namely:

$$\epsilon = \epsilon_0 \left(\epsilon_r + i \frac{\sigma}{2\pi \nu \epsilon_0} \right) \tag{2}$$

where ϵ_0 is the electrical permittivity of vacuum, ϵ_r is the dimensionless relative permittivity, σ is the conductivity in S/m, and ν is the frequency in Hz. This quantity had been measured on site for different soil moisture condition corresponding to both dry and wet soil (see Table 1). We use this one-layer model as our baseline one since it is simple and relatively immune to numerical artefacts. We simulate the three different ground planes – 3 × 3, 10 × 10, and serrated – described in Section 2.1 and Fig. 1.

2.4.2 *Measurement driven three-layer modelling*

We update the modelling just described adding the new available measurements for the soil complex permittivity. In constructing our first layered geometrical model, we adopted values at the nominal depths of Table 1, according to Section 2.2. A thickness was also chosen for the simulated layers according to the measurement depths, and we ensemble averaged the permittivities of the available measurements.

Note that the thickness of these three consecutive layers does not match the standard numerical accuracy criteria required by EM solvers. Despite this, we use these measurements to construct a three-layer soil model for the FEKO simulation ('measurements' column of Table 2).

2.4.3 *Numerical EM driven multi-layer modelling*

The thicknesses of the three-layer model are imposed by the depth of the available measurements and might not be sufficient for accurately representing a varying soil permittivity gradient. In order to solve the possible numerical issues connected to the thicknesses of the three-layer model, we refine our electromagnetic simulations using more layers. Although the separation between two consecutive layers is subject to different discretization rules according to each method, requesting a separation smaller than λ/10 is a widely used criterion. The standard FEKO method for any multi-layer substrate is a planar Green's function analytical solution embedded in the MoM

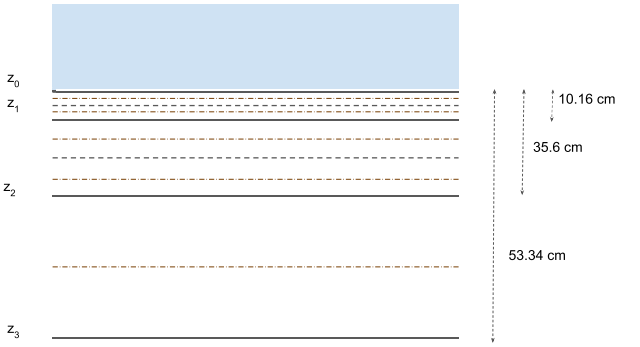

Figure 2. A 2D schematic view of the multi-layer splitting of soil half-infinite space $z < 0$, described in Section 2.4. A number of different measurements were made at three specific depths 10 per cent (10.16 cm, 35.56 cm, and 53.34 cm) and then ensemble averaged. A numerical EM driven multi-layer modelling is then constructed with an iterative sub-layering scheme. See text and Algorithm 1 for details.

formalism. A continuously varying permittivity is treated by means of properly discretising in layers, and a transmission line Green's function (TLGF) approach is used by the solver. Details for this can be found in Michalski & Mosig (1997).

When considering the λ/10 rule to discretize the half-infinite space, we have to take into account the different phase velocity which implies a different wavelength in each layer. For a low-loss medium, such as soil ($\sigma \ll 2\pi \nu \epsilon_0$ when considering our available measurements), the phase velocity is $c_p = c_0/\epsilon_r$, where c_0 is the speed of light in vacuum. We shall split each of the previous three layers into sub-layers such that their thickness is less than or equal to $\lambda_p/10$, and then double these layers iteratively until a certain convergence criterion is satisfied. The algorithm which implements this iteration is presented in Algorithm 1. In each iteration, we interpolate linearly to compute the new values of complex permittivity (`linInterp`), we merge them with the values of the previous iteration (`merge`), and we run a new FEKO simulation to calculate the gain pattern (`Gain`). More details on the choice of the sub-layering scheme are explained in Appendix A.

This iteration is applied both for relative permittivity and for conductivity in a square lattice fashion, and a maximum frequency $\nu_{\rm max} = 100$ MHz is used which provides a strong bound. By performing the first step of discretization, we conclude that each of the previous three layers of the dry soil should be divided into one or two sub-layers (see the grey dashed lines in Fig. 2). We then follow an iterative splitting by doubling these sub-layers (red dot–dashed lines in Fig. 2), in order to make an ever finer discretization. Wet soil conditions require a slightly finer splitting and are not reported in the schematic figure. The number of sub-layers used in the first iteration is reported in Table 2.

The iterative algorithm stops when a convergence threshold for the value of the gain at zenith is satisfied. We choose 0.1 dB which should be roughly similar to the numerical accuracy of FEKO. The number of layers needed for convergence are 40 and 56 layers for dry and wet conditions, respectively. The high number of layers to reach convergence is needed only for the serrated case but we assume it for all ground planes for convenience. We refer to this implementation as the converged model. Table 2 summarizes the different multi-layer approaches listing their number of layers. Fig. 3 shows the gain differences (in dB) between the converged case and the solution obtained with a smaller number of layers at all previous iterations. The analysis is repeated for all three different

$[\epsilon] \leftarrow [\epsilon_1, \epsilon_2, \epsilon_3]$;
$[\lambda_p] \leftarrow \frac{c_0 \epsilon_0}{\nu_{\max} \Re\{[\epsilon]\}}$;
$[\Delta\epsilon] \leftarrow [\epsilon_1, \epsilon_2 - \epsilon_1, \epsilon_3 - \epsilon_2]$;
$[N] \leftarrow [1, 1, 1]$;
$G_0 \leftarrow \text{Gain}([\epsilon])$;
for $i = 0, 1, 2$ **do**
  $N_{init} \leftarrow \left\lceil \frac{|z_{i+1} - z_i|}{[\lambda_p]_{i+1}/10} \right\rceil$;
  $[\Delta\epsilon]_{i+1} \leftarrow \frac{[\Delta\epsilon]_{i+1}}{N_{init}}$;
  $[N]_{i+1} \leftarrow N_{init}$;
  $[\epsilon] \leftarrow \text{merge}([\epsilon]_{1:i}, \text{linInterp}([\epsilon]_{i+1}, [N]_{i+1}, [\Delta\epsilon]_{i+1})$;
end
$G_1 \leftarrow \text{Gain}([\epsilon])$;
while $|G_1 - G_0| > 0.1$ *dBi* **do**
  $G_0 \leftarrow G_1$;
  for $i = 0, 1, 2$ **do**
    $[\epsilon] \leftarrow \text{merge}\ ([\epsilon]_{1:[N]_i - 1}, \ldots$
      $\text{linInterp}\ ([\epsilon]_{[N]_i:[N]_{i+1}-1}, 2[N]_{i+1}, [\Delta\epsilon]_{i+1}/2))$;
  end
  $[\Delta\epsilon] \leftarrow \frac{[\Delta\epsilon]}{2}$;
  $[N] \leftarrow 2[N]$;
  $G_1 \leftarrow \text{Gain}([\epsilon])$
end

Algorithm 1: Sub-layer splitting algorithm (see also Fig. 2) to achieve gain at zenith convergence of 0.1 dBi. [arg] indicates a vector-valued argument, while a subscript is used to index these values ($i_1 : i_2$ also indicates parsing from initial index i_1 to final index i_2). See text and appendix for details.

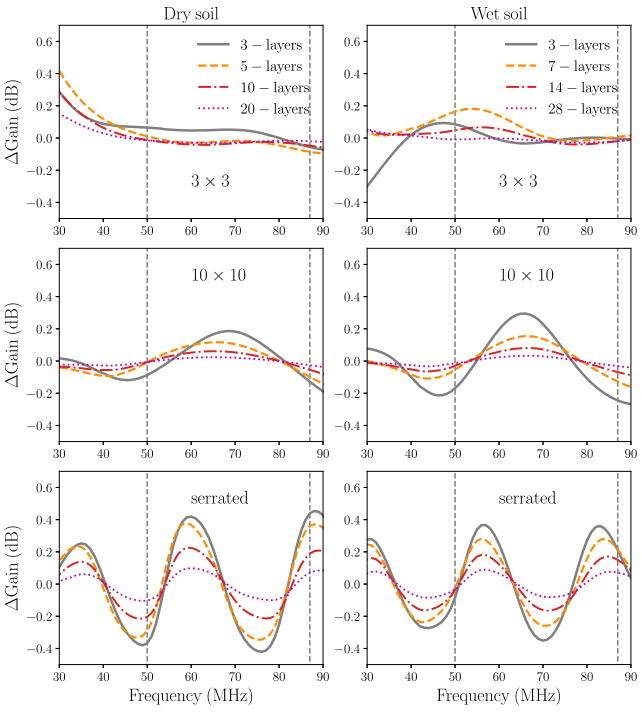

Figure 3. Gain at zenith dB difference of multi-layer implementations, calculated between the converged solution with 40 and 56 layers for dry and wet soil conditions, respectively, and solutions with fewer layers. Six cases are examined: different types of soil conditions (dry, wet) and different types of ground plane 3 × 3, 10 × 10, serrated). The vertical dashed lines highlight the region where LEDA data are available.

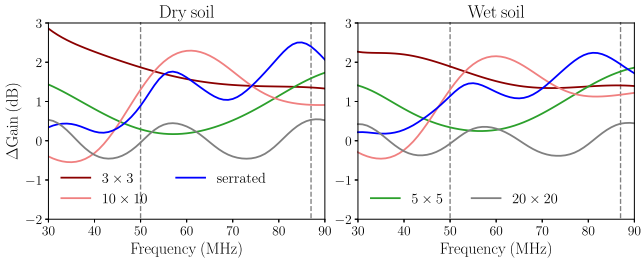

Figure 4. Gain at zenith dB difference of ground plane implementations, calculated between a reference model of an infinite PEC plane and the converged model of each ground plane as reported in the legend, for dry and wet soil conditions, respectively. An intermediate case of a 5 × 5 ground plane and a large 20 × 20 one, not examined elsewhere, are also shown. The vertical dashed lines in each panel highlight the region where LEDA data are available.

ground planes. We note the existence of periodic oscillations for the case of the 10 × 10 ground plane, with or without serrations. This fact highlights that successive implementations of sub-layers differ roughly by sinusoidal factors, which are still present when the ground plane gets bigger. This is a counter-intuitive conclusion, which might originate from sharp permittivity value transitions between consecutive layers (expressed in boundary conditions of the TLGF). The 3 × 3 ground plane performs better with respect to the oscillation, apart from a low-frequency drift off.

2.4.4 Finite size of the ground plane

Oscillation effects are also observed when comparing all finite sized ground planes with respect to an infinite perfect electric conductor (PEC) plane solution. To demonstrate this, in Fig. 4 we subtract from the converged case the solution for an infinite PEC plane, for each of the considered ground planes. We also include a 5 × 5 and a 20 × 20 ground plane, as an intermediate and extreme case. The sinusoidal variations that can be seen imply that there are finite-size truncation/diffraction effects which need long electrical distances (i.e. distances as multiples of λ) to diminish. The amplitude and periodicity of these oscillations are different for each ground plane and depend on their size.

Having examined the effect of different ground planes, soil conditions as well as soil layering options, a comparative plot of zenith gain can best illustrate their effects before any chromaticity correction is calculated. For each ground plane and soil conditions, we present in Fig. 5 the baseline one-layer, the three-layer, and the converged multi-layer FEKO model. As expected, the 3 × 3 ground plane provides in most cases a lower gain, since there are more losses related to the part of the soil not covered by the ground plane. It is, however, the best one in terms of ground plane induced ripple, which has a lower frequency due to its smaller dimension. Note that concerns over the spectral structure of an underlying ground plane have already been addressed in other experiments such as SARAS3 (Jishnu Nambissan et al. 2021; Singh et al. 2021) that moved the antenna on a lake to minimize the chromatic response. The MIST experiment has opted instead for not deploying a ground plane and carefully characterize the ground properties. For an antenna configuration less sensitive to the ground properties than LEDA (which is facing downwards and is more coupled to any underlying structure), a larger ground plane is also expected to alleviate the problem. The EDGES team, for example, has used a 30 × 30 ground plane for their results (Bowman et al. 2018).

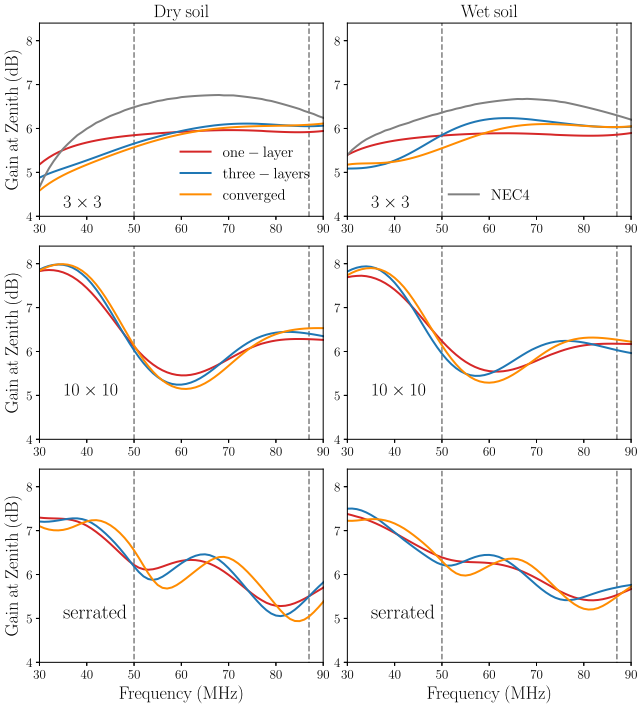

Figure 5. Gain at zenith of different multi-layer implementations, including the baseline model, a three-layer model, and the converged multi-layer model (40 and 56 layers for dry and wet soil conditions, respectively). Six cases are examined, as in Fig. 4. For the 3 × 3 ground plane, the NEC4 simulated model is also shown. The vertical dashed lines in each panel highlight the region where LEDA data are available.

We include in Fig. 5 for comparison the 3 × 3 ground plane solution obtained with the NEC4 pattern used in previous analysis. The NEC4 patterns have been scaled down using the radiation efficiency as calculated with FEKO data (see the next paragraph) since the NEC4 model was overestimating the gain by omitting the inclusion of soil losses in its gain calculation (Weiner 1991). Despite this correction, the FEKO and NEC4 models differ by a factor of up to 1 dB across the frequency range of interest, a result that showcases the differences between numerical solvers.

2.4.5 *Radiation efficiency*

We present here the radiation efficiency $\eta_{\rm rad}$ as a function of frequency, which takes into account losses over all of the 3D antenna pattern. The radiation efficiency is calculated using the integral of the upper hemisphere far field patterns and the input power at the antenna port, given by FEKO. In Fig. 6, $\eta_{\rm rad}$ is shown for the three examined ground planes. As expected, the 3 × 3 ground plane presents more losses, with a clearer frequency dependence as well, since the efficiency is poorer at lower frequencies. A 10 × 10 ground plane with or without serrations is more appropriate to keep losses smaller than 10 per cent in most of the frequency band, and quite more stable at the extremes, as they have a larger extent and allow for more power radiated below the horizon (>90°) to be reflected back, contributing to the gain. The radiation efficiency is not constant and this affects the gain integral which is not 4π and varies with frequency. The beam integral is expected to vary significantly in the case of 3 × 3 ground planes, such that any normalization of the beam pattern should be made separately for each frequency (see also Section 3.2).

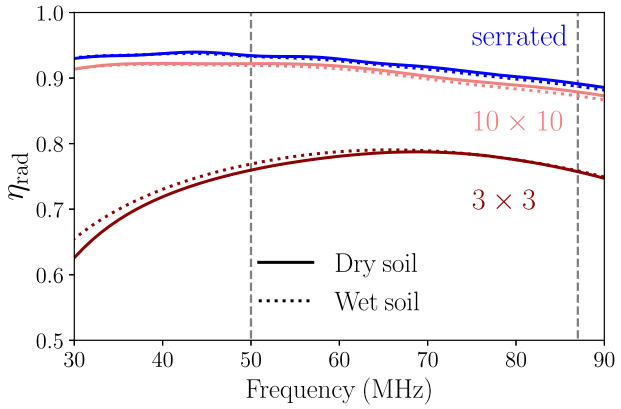

Figure 6. Radiation efficiency over frequency calculated for the three different cases of ground plane, using the FEKO solution outputs. Dry (solid lines) and wet (dotted lines) conditions for the baseline one-layer model are presented. The vertical dashed lines highlight the region where LEDA data are available.

2.4.6 *Beam gain variation*

As a final assessment of the radiation pattern spectral robustness, we present a number of 2D colour-maps of the beam dB change in gain with respect to frequency in Fig. 7, for 4 azimuth angles $\phi = 0°$, 30°, 60°, 90°, a criterion similar to that evaluated by Mahesh et al. (2021). This kind of plot is useful not only to confirm the sinusoidal-factor spectral periodicity due to the ground plane structure, but any other spatial effects which predominantly appear across zenith angle θ. It can be seen from the figure that these spatial variations are significant even for $\theta < 40°$, which compares with the half-power beam width of the antenna. Another interesting phenomenon is that the 'phase' of this sinusoidal-factor variation is different for each elevation, which means that any analytic approach such as that of equation (1) with $\theta \times \cos(\theta)$ polynomial terms is not adequate to describe the complexity of the beam pattern.

The amplitude in azimuth angle diminishes when we cross from the *E*-plane ($\phi = 0°$) to the *H*-plane ($\phi = 90°$). The greatest variation both in terms of amplitude and number of complete cycles in the frequency range of interest is found for the serrated ground plane, which reaches as high as 0.2 dB/MHz in many ν–θ sample points.

3 SIMULATED OBSERVATIONS

In this section, we describe the construction of LEDA mock measured spectra, the correction factor for the beam-induced chromaticity of the simulated spectra and discuss qualitatively its impact on the accuracy of the smooth foreground model. As we already mentioned, we make use of a baseline, single-layer model, since the previous analysis has shown that the three-layer and multilayer models suffer from some uncertainties: lack of more measurements for the former, and interpolations assumptions for the latter.

3.1 Modelling the sky observed temperature

In order to simulate the spectra measured by LEDA, we compute the beam-averaged sky brightness temperature as seen by a single antenna $T(\hat{\boldsymbol{n}}_0, \nu, t)$ at the time t and direction $\hat{\boldsymbol{n}}_0$ (e.g. Bernardi et al. 2015):

$$T_{\rm obs}(\hat{\boldsymbol{r}}_0, \nu, t) = \frac{\int_\Omega B(\hat{\boldsymbol{n}}', \nu)\, T_{\rm sky}(\hat{\boldsymbol{n}}', \nu, t)\, {\rm d}\hat{\boldsymbol{n}}'}{\int_\Omega B(\hat{\boldsymbol{n}}', \nu)\, {\rm d}\hat{\boldsymbol{n}}'} + T_{\rm N}(\nu) + T_{21}(\nu) \quad (3)$$

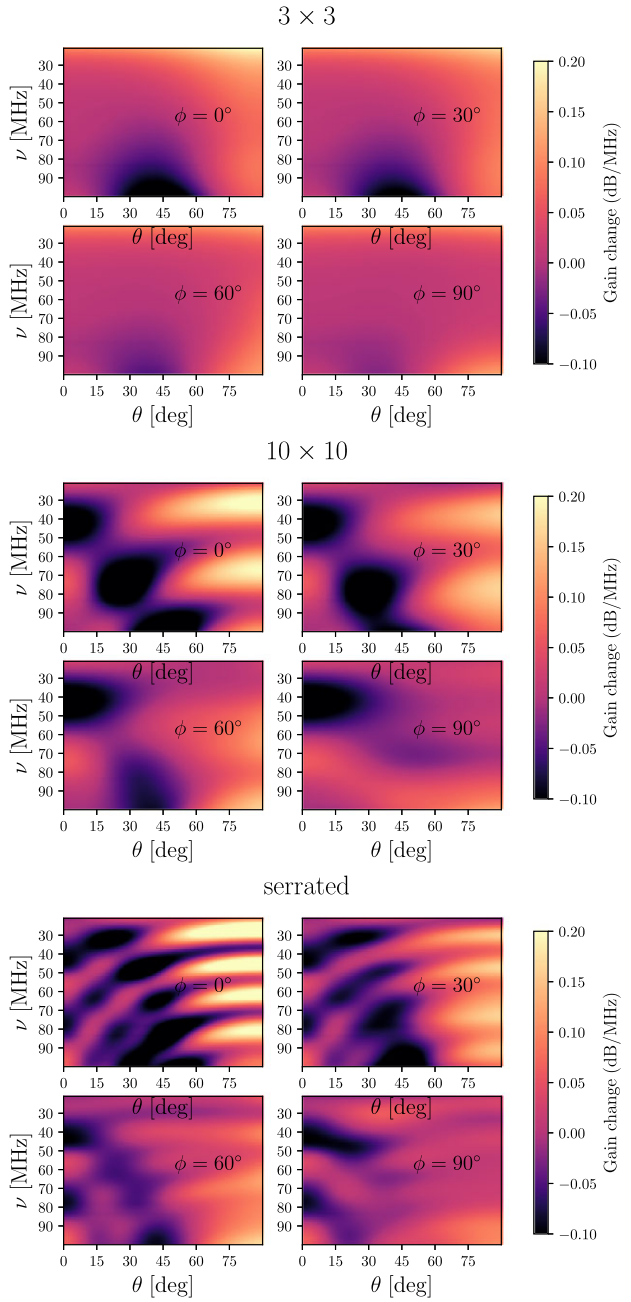

Figure 7. Beam gain change per unit frequency as a function of the angle θ and for four selected ϕ values (0°, 30°, 60°, and 90°). We show here the one-layer model for dry soil condition.

where B is the antenna gain pattern and $T_{\rm N}$ the instrumental noise. $T_{\rm sky}$ is the sky brightness temperature, which changes with time as the sky drifts over the dipole. To model this latter, we simply consider the Haslam 408 MHz full-sky map $T^{\rm H}(\hat{\mathbf{n}})$ (Haslam et al. 1982) and scale it to different frequencies assuming a constant spectral index β

$$T^{\rm H}_{\rm sky}(\nu, \hat{\mathbf{n}}) = [T_{\rm H}(\hat{\mathbf{n}}) - T_{\rm cmb}] \left(\frac{\nu}{408}\right)^{\beta} + T_{\rm cmb}. \quad (4)$$

where $T_{\rm cmb} = 2.725$ K and $\beta = -2.5$. Note that other different sky models such as the GSM (Zheng et al. 2016) or the GMOSS (Sathyanarayana Rao et al. 2017) could be considered, including the effect of a spatially varying spectral index. Nevertheless, in this work

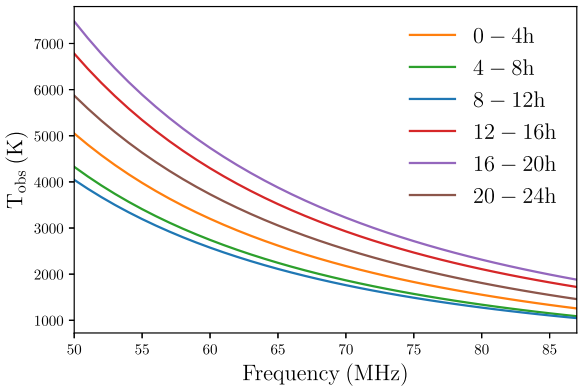

Figure 8. Simulated antenna temperature as seen through the LEDA beam as a function of frequency in the 50–87 MHz range. The different colours correspond to different 4 h LST bins.

we are mainly interested in varying the antenna simulations and we postpone the investigation of sky modelling uncertainties to a future work. Moreover, due to the large beam, a spatially constant spectral index is a reasonable approximation (Cumner et al. 2022).

We show the resulting antenna temperature averaged over 4 h LST bins in Fig. 8, that can be compared to fig. 13 in Mahesh et al. (2021) and shows the low foreground contamination in the LST range 8–12 h, corresponding roughly to the chosen one for our data analysis in Spinelli et al. (2021).

We model the 21-cm global signal $T_{21}(\nu)$ with a Gaussian absorption profile (Bernardi et al. 2015; Presley, Liu & Parsons 2015; Bernardi et al. 2016; Monsalve et al. 2017):

$$T_{21}(\nu) = A_{21}\, e^{-\frac{(\nu-\nu_{21})^2}{2\sigma^2_{21}}}, \quad (5)$$

where A_{21}, ν_{21}, and σ_{21} are the amplitude, peak position, and standard deviation of the 21-cm trough, respectively. This is an approximation and more realistic shapes for the absorption feature could be computed from numerical or semi-analytical simulations (e.g. Mirocha 2014; Mirocha, Harker & Burns 2015; Cohen, Fialkov & Barkana 2016; Cohen et al. 2017; Mirocha, Furlanetto & Sun 2017; Reis et al. 2021), however, analytic expressions are useful for fast evaluation of likelihood functions. We adopt in this work a simplistic assumption for the signal strength using $A_{21} = -180.0$ mK, $\nu_{21} = 70$ MHz, and $\sigma_{21} = 2$ MHz. We do expect our results to be dependent on the parameters chosen for the signal. With these values, the absorption profile is narrow (i.e. easier to disentangle from the smooth foregrounds) and well inside our observed band. In this study we are, however, mostly interested in relative behaviours for the beam modelling allowing us to fix the input cosmological model. We discuss this approximation further in Appendix B.

In order to limit the parameter space to explore, we construct mock data as faithful as possible to the actual LEDA data (see Spinelli et al. 2021) and we construct the mock spectra $\bar{T}_{\rm ant}(\nu)$ by averaging equation (3) in the LST range 8.5–12 h.

To compute the noise T_N, we assume that it is given by the radiometer equation and it is uncorrelated in frequency and time. We assume that for each frequency channel it follows a Gaussian distribution with standard deviation:

$$\sigma^N(\nu) = \frac{\bar{T}_{\rm ant}(\nu)}{\sqrt{\Delta t\, \Delta\nu}}, \quad (6)$$

where we consider a $\Delta\nu = 1$ MHz channel width and a $\Delta t = 100$ h of total integration time, in agreement to real LEDA data specifics.

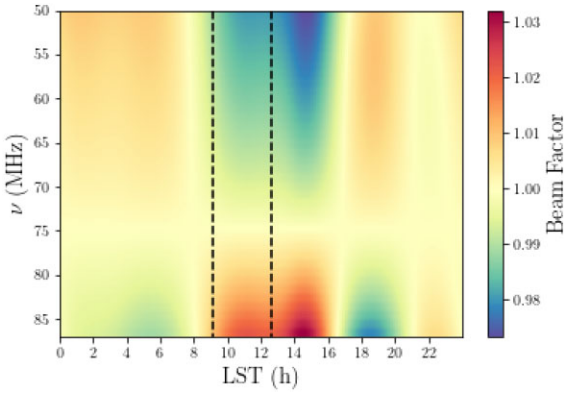

Figure 9. The chromaticity correction (equation 7) computed using the sky model of equation (4) and the baseline beam model from FEKO (one-layer, dry soil) considering the 3 × 3 m ground plane. The dashed vertical lines highlight the LST range preferred for LEDA data analysis.

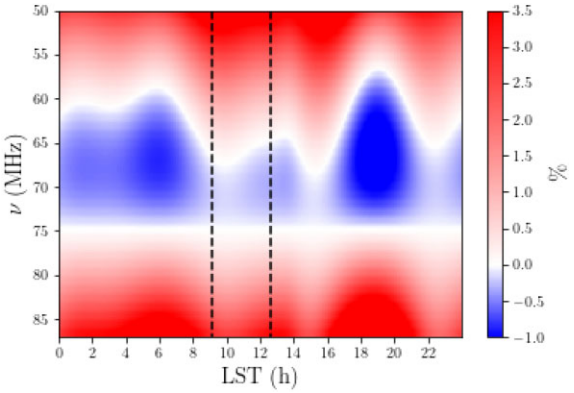

Figure 10. Percentage difference between the chromaticity correction factor B_c (equation 7) computed for the new baseline beam model and the analytic beam used in previous analysis. The dashed vertical lines highlight the LST range preferred for LEDA data analysis.

3.2 Chromaticity correction

Assuming a well-behaved beam with a small degree of chromaticity, the resulting spectra of equation (3) are expected to be smooth in frequency. Although not visible by eye in Fig. 8, realistic beam shapes induce a non-smooth frequency structure in the measured sky temperature that, as we will discuss more extensively later on, complicates the signal reconstruction. As discussed in other works (e.g. Anstey et al. 2020; Monsalve et al. 2020; Mozdzen et al. 2019), a possible approach to alleviate the effect of the chromatic beam on the measured spectra is to correct the original spectra using the following factor:

$$B_c(\nu, \mathrm{LST}) = \frac{\int_\Omega T_{\mathrm{sky}}(\nu_0, \mathrm{LST}, \hat{\mathbf{n}}')B(\nu, \hat{\mathbf{n}}')\mathrm{d}\hat{\mathbf{n}}'}{\int_\Omega T_{\mathrm{sky}}(\nu_0, \mathrm{LST}, \hat{\mathbf{n}}')B(\nu_0, \hat{\mathbf{n}}')\mathrm{d}\hat{\mathbf{n}}'} \frac{\int_\Omega B(\nu_0, \hat{\mathbf{n}}')\mathrm{d}\hat{\mathbf{n}}'}{\int_\Omega B(\nu, \hat{\mathbf{n}}')\mathrm{d}\hat{\mathbf{n}}'}. \quad (7)$$

Note that T_{sky} is a function of LST since the sky drifts with time over the antenna. We choose $\nu_0 = 75$ MHz as a reference frequency (Mozdzen et al. 2019) since it is approximately central in our range. In this formulation it should also be pointed out that the beam pattern $B(\nu, \hat{\mathbf{n}}')$ used is gain, so the second term on the right hand side of the equation is $\eta_{\mathrm{rad}}(\nu)/\eta_{\mathrm{rad}}(\nu_0)$.

We compute the beam chromaticity correction using the various beam models presented in Section 2. Note that we consider LST bins of 10 min and the full 24 h range for completeness when computing the correction. Since our goal is to investigate the effect of the beam, we use the same sky model of equation 4 to disentangle the two effects and to avoid introducing complications due to a different sky model than the one assumed to compute the simulated spectra. An example of the correction is reported in Fig. 9 where we show our baseline case of one-layer, dry soil conditions, and 3 × 3 m ground plane (see Section 2).

It is interesting to evaluate, as shown in Fig. 5, the difference between the analytic beam model previously used and the new FEKO baseline simulation, computing the chromaticity correction. This is reported in Fig. 10. Differences reach a few per cent especially around LST ∼ 18, when the Galactic Centre is transiting.

We can repeat the same exercise for the various FEKO beam models computed for this analysis. We show in Fig. 11 the difference between the dry and wet soil conditions for the three different ground planes. Differences are a fractional of per cent but their structure present different patterns for different ground plane shapes (see Figs 3 and 5). The same structure of periodic peaks/troughs across frequency is seen in each constant LST line, as was observed for the dry/wet layer simulation, as well as the sub-layer convergence study. There is additionally a variation along LSTs in constant frequency lines that has to do with the beam coupling to a fainter/brighter sky.

In Appendix C, we report for completeness the resulting chromaticity difference arising from small variation in soil properties and for the multi-layer parametrization discussed in Section 2.4.

3.3 Mock data modelling

To construct a model for our mock data we assume that the Galactic foreground spectrum can be described as a N-term log-polynomial (e.g. Bowman & Rogers 2010; Pritchard & Loeb 2010; Harker et al. 2012; Bernardi et al. 2015; Presley et al. 2015; Bernardi et al. 2016):

$$\log_{10} T_{\mathrm{fg}}(\nu) = \sum_{n=1}^{N} p_{n-1} \left[\log_{10}\left(\frac{\nu}{\nu_0}\right)\right]^{(n-1)} \quad (8)$$

with $\nu_0 = 60$ MHz. Note that p_1 corresponds to the spectral index β of equation (4), since for $N = 2$ we can rewrite equation (8) as $T_{\mathrm{fg}}(\nu) = p_0(\nu/\nu_0)^{p_1}$.

We are interested in assessing the impact of the beam chromaticity on this assumption, examining its effect on the frequency smoothness of our simulated spectra computed as in equation (3) and assuming no absorption feature, i.e. $T_{\mathrm{HI}} = 0$. We compute the deviation of the mock measured sky temperature with respect to the smooth foreground model of equation (8). Note that the best-fitting values for the foreground parameters are obtained with a non-linear least squares solver.

We first analyse the ideal case of an infinite ground plane for completeness. This antenna pattern is an ideal case which has only been used as reference for subtraction in Fig. 4, and produces the smoothest spectral response for gain. We show in the top panel of Fig. 12 that the log-polynomial model with $N = 6$ is already capable of describing the spectra very well, in particular for LST < 8 h. A higher log-polynomial order is required instead for the LST range of the 2018/2019 LEDA observing campaign (i.e. 9–12 h). When the beam modelling includes the finite ground plane (the 3 × 3 ground plane is shown as an example in the bottom panel of Fig. 12) there are residual structures that are not captured by the model of equation (8). These residuals again depend on the LST range considered, as the beam couples with the sky structures.

We investigate this further as a function of the ground plane type in Fig. 13, where we use our baseline case, i.e. the dry soil one-layer

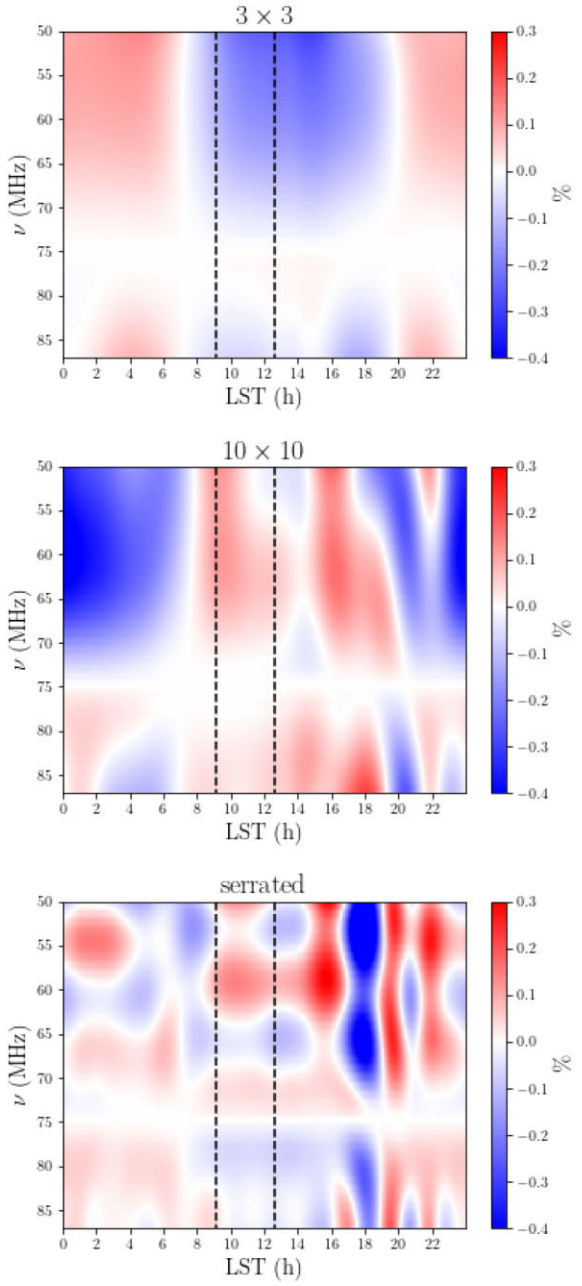

Figure 11. The difference in percentage between the chromaticity correction factor B_c of equation (7) computed for dry and wet soil conditions. We consider here the one-layer FEKO model and we compute the difference for the various ground planes: 3 × 3 m (top panel), 10 × 10 m (middle panel), and serrated (bottom panel). The dashed vertical lines highlight the LST range preferred for LEDA data analysis.

model. If we do not correct for the effect of beam chromaticity, the induced structures in the spectra prevent the smooth model from accurately describing the foregrounds, and the residuals are highly oscillating in frequency. The rms values for the results can be found in Table D1 for different choices for the order of the log-polynomial. The effect is more prominent for the serrated ground plane (where we found residual rms values around 1 K) and still important for the 10 × 10 ground plane. An exact chromaticity correction solves the problem for all types of ground planes describing the resulting simulated spectra with residuals of only a few mK.

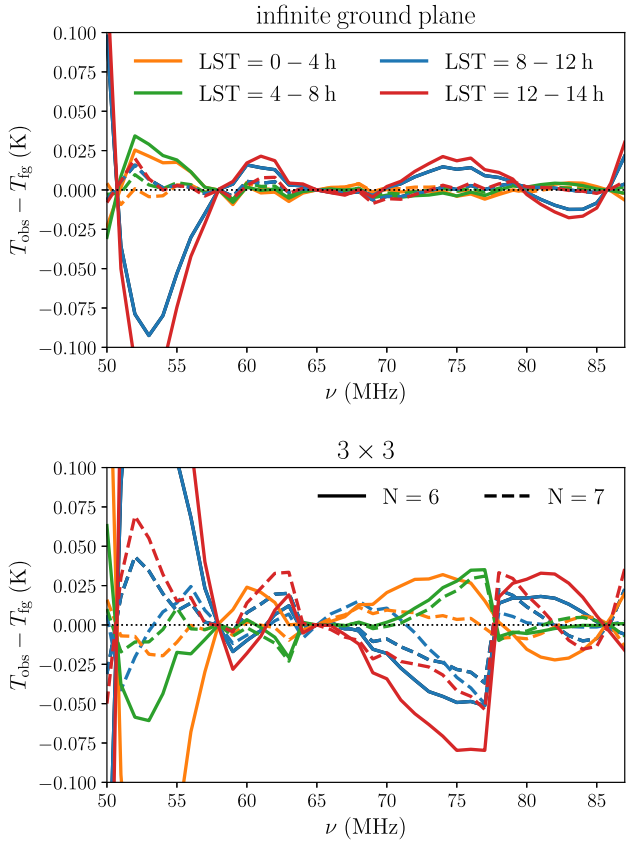

Figure 12. Residual difference (in K) as a function of frequency between the simulated spectra of equation Section 3 and the best-fitting model of equation (8), presented for different orders of the log-polynomial ($N = 6$ in solid lines and $N = 7$ with dashed lines) and for different LST bins. Different ground planes are considered: an ideal infinite ground plane (top panel) and the 3 × 3 ground plane (bottom panel). Note that the residual are computed without any chromaticity correction.

If we attempt a correction assuming wet properties for the soil parameters instead of dry conditions, we obtain better residuals but still with strong features as a function of frequency.

We repeat this same analysis considering now the impact of the multi-layer description of the soil. We show in Fig. 14 the residual structures for the baseline model (one-layer, dry soil condition) when correcting the effect of chromaticity assuming either the three-layer or the converged multi-layer model, for different N-term log-polynomial models (5, 6, and 7), and different ground planes (3 × 3, 10 × 10, and serrated). The rms of the residuals are reported in Table D2 in Appendix D. Note that the non-corrected and the exact correction cases are the same of Fig. 13.

Attempting a chromaticity correction with the three-layer model (that is similar to the baseline one) always improves the rms and the smoothness of the resulting spectra. The converged layer model instead worsens the structures in the residuals and, for the serrated case, there is very small improvement increasing the order of the log-polynomial model. These results can be compared with Fig. C2. Despite the differences in the chromaticity patterns between the three-layer and the converged layer cases not being strong, the higher contrast of the structures in the right column of Fig. C2, foreshadows the possible struggles of the correction procedure for the converged case.

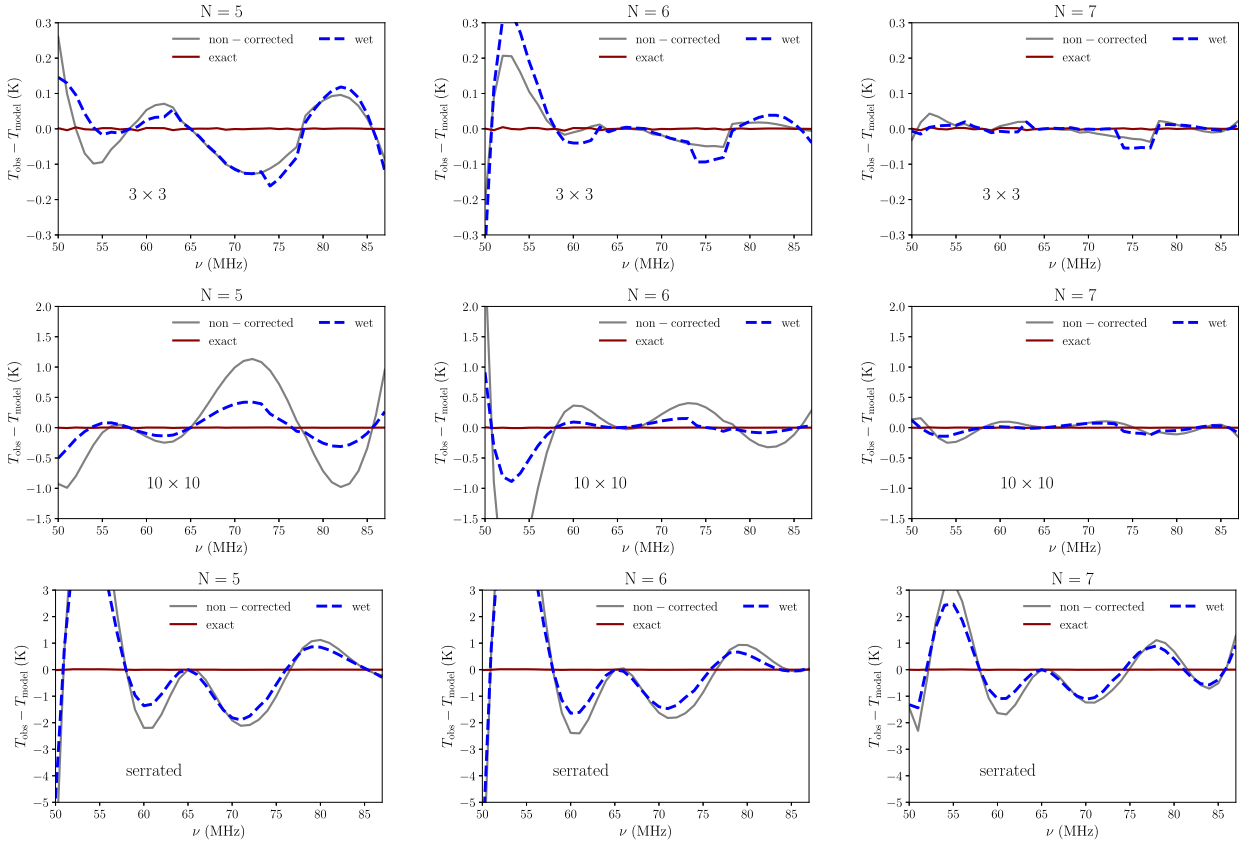

Figure 13. Residual difference (in K) as a function of frequency between the best-fitting model of equation (8) and the simulated spectra obtained as described in Section 3.1, presented for different polynomial orders ($N = 5$, 6, 7, left-hand, central, and right-hand panels, respectively) and for different ground planes (3×3 top panels, 10×10 central panels, and serrated bottom panels). The simulated spectra are obtained considering dry condition and a one-layer description for the soil. The residuals are then computed without any chromaticity correction (grey solid lines), with an exact correction using the same beam model as for the spectra in input (dark red solid line) and for a chromaticity correction computed with wet soil condition (blue dashed lines). Note that the vertical scale changes for the different ground plane examined. Rms value for these residuals can be found in Table D1.

We can, in each case, confirm that the presence or not of a ground plane is more important than the parametrization of soil both for dry/wet conditions and different layer models, since the residuals are high for the more oscillating larger ground planes, and these oscillations are inherent to the antenna pattern as a function of frequency.

These type of structures in the real data could prevent the detection of the cosmological signal or produce an erroneous detection and thus need to be investigated further. The rest of this work is dedicated to this problem.

4 FOREGROUND AND COSMOLOGICAL PARAMETER RECONSTRUCTION

In the last session, we have discussed qualitatively the impact of a realistic beam model for the LEDA antennas, which can compromise the smoothness of the measured spectra, and is thus an important assumption for discerning the 21-cm signal from the foregrounds.

In this section, we investigate how much these spurious structures in the simulated spectra impact the Bayesian extraction of the 21-cm absorption feature (e.g. Bernardi et al. 2016; Bowman et al. 2018; Singh et al. 2021).

Our results were obtained running the HIBAYES code (Bernardi et al. 2016; Zwart, Price & Bernardi 2016), a fully Bayesian framework where the posterior probability distribution is explored through the MULTINEST sampler (Feroz & Hobson 2008; Feroz, Hobson & Bridges 2009). We assume a Gaussian likelihood for the data and make use of the model described in Section 3.3. The covariance matrix is assumed diagonal in frequency and the diagonal terms are computed with equation (6). For each analysed case we run the pipeline for different order of the log-polynomial and present the results with the highest evidence.

4.1 Finite ground plane effect

We analyse the structure induced on the simulated spectra by the different ground planes used in LEDA observations and modelled in this work. We show in Fig. 15 the reconstructed T_{HI} obtained from the mean values of the posterior distributions, in comparison with the input HI model used for the simulated spectra. While for an infinite ground plane it is possible to reconstruct the correct input, in presence of a finite ground plane, the algorithm converges towards biased solutions, preventing a correct detection of the cosmological signal. In Fig. 15 no correction for the effect of chromaticity is applied. If we divide the simulated spectra with the beam factor of equation (7), computing it with the same beam model used for the simulated spectra, we are exactly correcting for the effect of chromaticity. The corrected spectra are much smoother as a function of frequency and they are well modelled by a low order of the log-polynomial. The input HI parameters are successfully reconstructed with residuals of the order of a few mK using only a 5-term polynomial model.

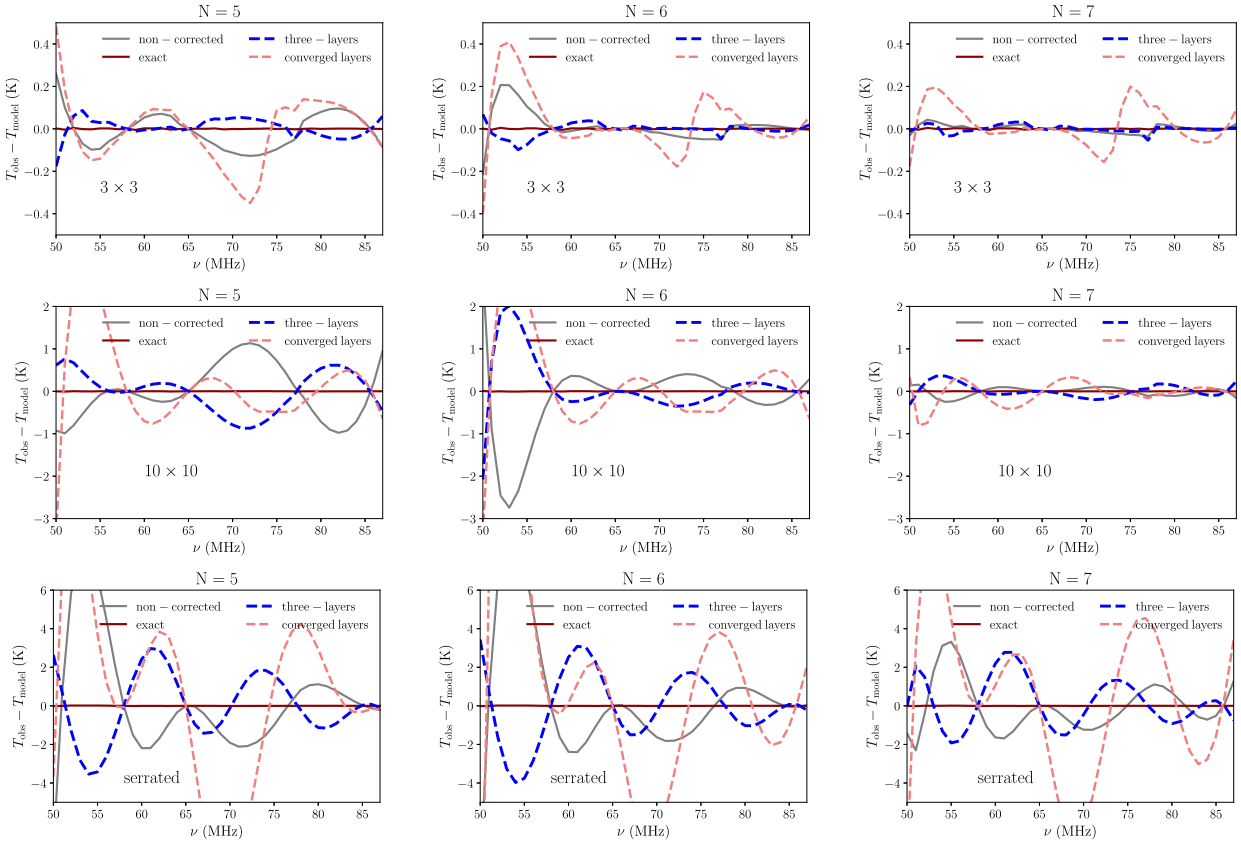

Figure 14. Residual difference (in K) as a function of frequency between the best-fitting model of equation (8) and the simulated spectra obtained as described in Section 3.1, presented for different polynomial orders ($N = 5$, 6, 7, left-hand, central and, right-hand panels, respectively) and for different ground planes (3×3 top panels, 10×10 central panels, and serrated bottom panels). The simulated spectra are obtained considering dry condition and a one-layer description for the soil. The residuals are then computed without any chromaticity correction (grey solid lines), with an exact correction using the same beam model as for the input spectra (dark red solid line), for a chromaticity correction computed instead with the three-layer model (blue dashed lines) or the converged layer model (pink dashed line). Note that the vertical scale changes for the different ground planes examined. Rms values for these residuals can be found in Table D2.

4.2 Soil properties

The results of the previous section suggest that, when attempting a reconstruction of the absorption feature in the LEDA data we need to correct for the effect of chromaticity. It is, however, not realistic to assume that our beam model agrees perfectly with the true beam. We investigate here the effect of a non-perfect reconstruction by varying the properties of the soil.

We analyse in Fig. 16, for the 3×3 ground plane, the effect on the reconstructed absorption feature of small variations in the assumed value for the conductivity (σ) or the permittivity (ϵ_r) of the soil. We consider a 10 per cent shift with respect to the dry soil condition to be compared with a factor $\sim$2 difference between the dry and wet condition (presented in Table 1). We report for completeness in Fig. C1 the variation of the beam factor in these analysed cases with respect to the baseline beam model. As can be seen also from Fig. 16, the change in conductivity biases the reconstructed absorption feature for both higher and lower values of σ. A lower value of the conductivity leads to a 20 per cent lower amplitude for the absorption signal while a higher conductivity bias the reconstruction of its central frequency. Increasing the permittivity has a similar effect while the bias gets stronger for a lower value of ϵ_r, resulting in a factor $\sim$2 enhanced amplitude. These results are consistent with Fig. C1. Note that a different assumption for the input model would have produced slightly different results. It is however still instructive to estimate the expected magnitude of the bias.

We investigate also a more drastic situation, where the soil conditions for the correcting chromaticity factor are the 'wet' case presented in Table 1 and Fig. 11. We report the reconstructed $T_{\rm HI}$ in Fig. 17. For the 3×3 ground plane, already analysed, the result is similar to the small variations in permittivity and conductivity just discussed, as could have been anticipated comparing the top panel of Fig. 11 with Fig. C1. The reconstruction is completely biased for the case of the larger ground planes, where the 'dry' and 'wet' chromaticity corrections present more structured differences (see the middle and lower panel of Fig. 11).

We analyse the impact of soil modelling further in Fig. 18 where we compare the three-layer and converged layer models against the baseline. As was hinted in Fig. 14, for the 3×3 case, the three-layer correction is better than no correction, while the converged layers description of the soil is already too much different from the one layer to offer better correction. The other ground plane cases show various biased results, proving that the correction is not solving the problem of the residual structures in the simulated spectra.

4.3 Spectral index reconstruction

While studying the correct reconstruction of the HI absorption feature, we also discuss the reconstructed foreground parameters. The most informative one is the spectral index β that can be compared with its input value -2.5 (see Section 3.1). We report the peak of the

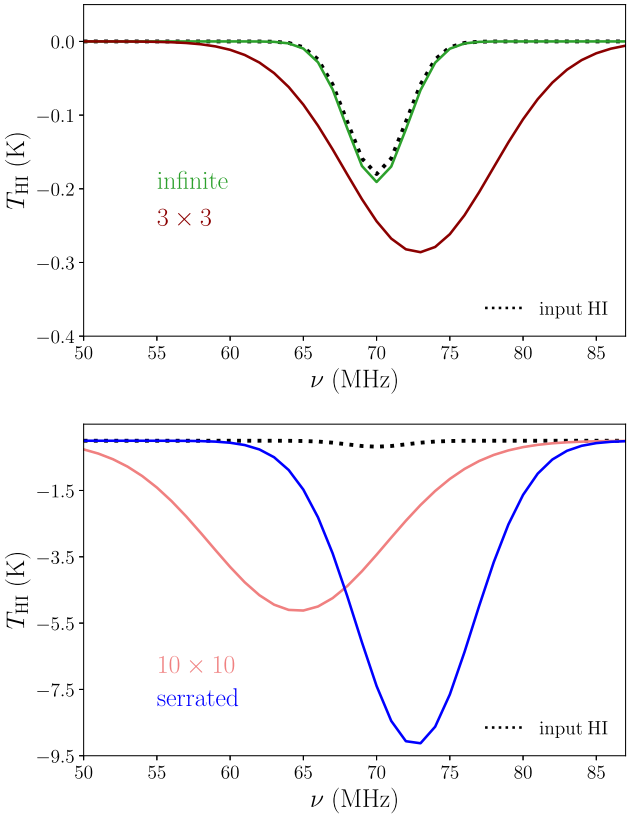

Figure 15. The reconstructed 21-cm absorption profile for different ground planes considered. In the upper panel the infinite case and 3 × 3 are shown in green and dark red, respectively. The 10 × 10 and the serrated cases are instead shown in the lower panel in pink and blue, respectively. Note the different scale for the *y*-axis. The simulated spectra are generated for the one-layer dry soil conditions and are not corrected for the effect of chromaticity. The input model that we would like to reconstruct is shown as a black dotted line. The serrated result is shown for completeness but the amplitude of the absorption feature converged to the edge of the prior.

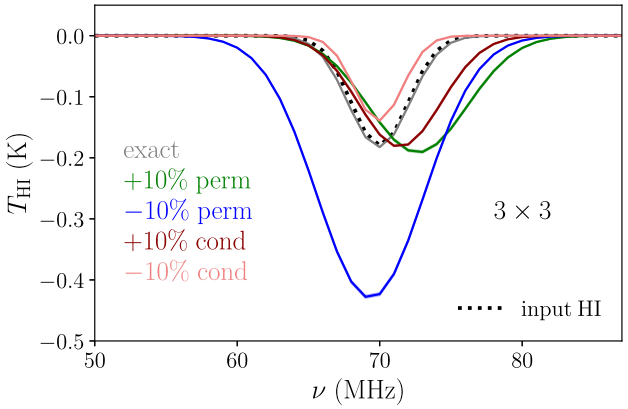

Figure 16. The reconstructed 21-cm absorption profile obtained when the simulated spectra (generated for the one-layer dry soil conditions) are corrected for the effect of chromaticity considering a ±10 per cent variation for the permittivity and conductivity. The input model that we would like to reconstruct is shown as a black dotted line.

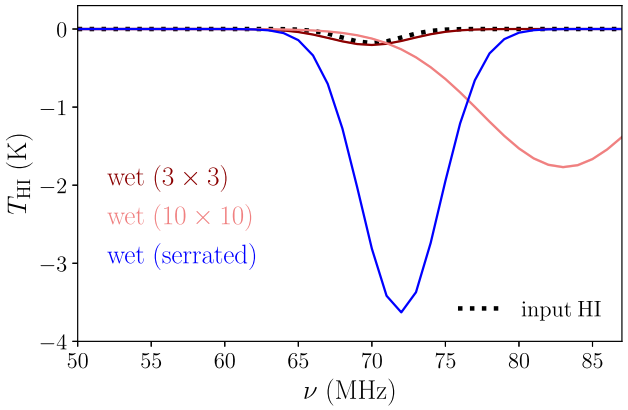

Figure 17. The reconstructed 21-cm absorption profile obtained when the simulated spectra (generated for the one-layer dry soil conditions) are corrected for the effect of chromaticity considering a wet soil moisture. We present the results for the three different ground planes considered (3 × 3 in dark red, 10 × 10 in pink, and the serrated case in blue).

posterior distribution of the spectral index for each case in Fig. 19. We find that, when we do not correct for the effect of chromaticity, we recover up to a 10 per cent flatter β. The effect is stronger for larger ground planes. We instead always recover the right spectral index for the exact correction, or when the beam factor is computed varying the soil moisture properties. Finally, there is a tendency for a slightly flatter β (a few per cent) when we use different multi-layer modelling. These flatter values of the spectral index are associated with strongly biased values of the amplitude of the absorption feature as can be seen in Figs 15 and 18.

5 DISCUSSION AND CONCLUSIONS

In this work, we presented the characterization of the LEDA antenna beam, with emphasis on the role of the ground plane and of the soil modelling both in terms of discretizing the semi-infinite volume it occupies, and varying its electromagnetic parameters. We used FEKO for our simulations and constructed a multi-layer model of the terrain relying on *in situ* measurements of the soil complex permittivity. We used a more standard one-layer model under dry/wet soil conditions as our baseline and discussed the variations in the absolute gain pattern. when exploring more sophisticated models. The characterization of the antenna beam is of primary importance in assuring an accurate enough control of the systematic effects in 21-cm global signal analysis and has been studied in detail for other experiments (e.g. Mahesh et al. 2021; Raghunathan et al. 2021).

We explored the impact of beam modelling uncertainties due to soil moisture on the antenna chromaticity, focusing on three different ground planes used in the actual LEDA observations (Spinelli et al. 2021): a 3 × 3 m, a 10 × 10 m, and a 10 × 10 m with 10 m long triangular serrations. The addition of the ground plane induces a frequency ripple in the beam pattern that compromises its smoothness. The ripple amplitude is smaller for larger ground planes while its oscillation frequency is larger. The amplitude of the ripple depends also, to a lesser extent, on the number of layers that describe the permittivity as a function of depth. However, this effect saturates for a sufficiently large number of layers.

We then compared the gain at zenith for values of the complex permittivity corresponding to dry or wet terrain at the LEDA site. Surprisingly, the impact of different soil conditions is not suppressed by the presence of a larger ground plane and appears as a slight shift in the oscillatory pattern. The shift is more evident for the serrated ground plane case and affects the full shape of the beam. This makes

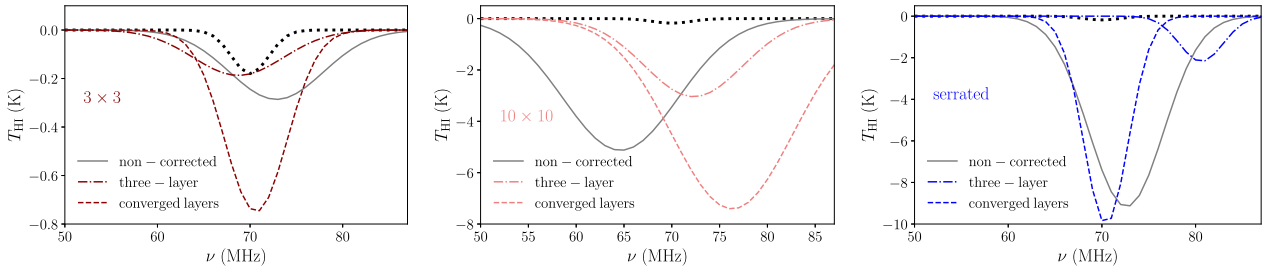

Figure 18. The reconstructed absorption profile for the 3 × 3 (left-hand panel), 10 × 10 (central panel), and serrated ground plane (right-hand panel) for the one-layer dry soil baseline case spectra, when we are correcting with a chromaticity factor computed using the three- or the converged layer model. Note the different vertical axis scale for the three panels. The dotted line is the input profile. For completeness, also the non-corrected case presented in Fig. 15 is shown in grey in each panel.

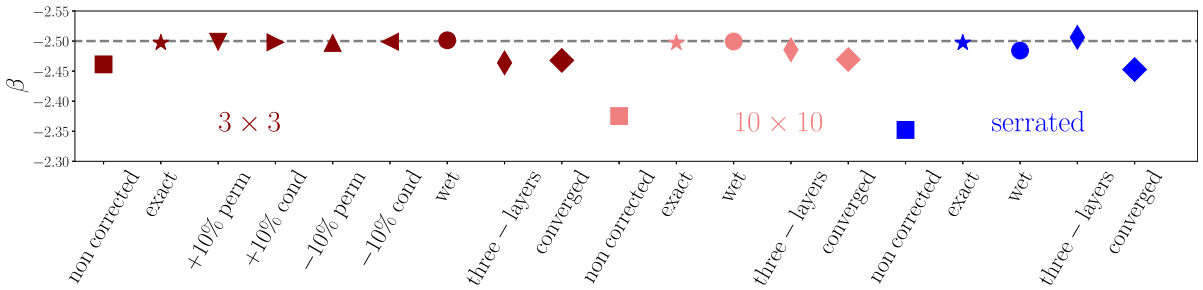

Figure 19. Mean value for the posterior of the spectral index β (corresponding to the second term of the log-polynomial model) for the different cases analysed in this work. The true input value of $\beta = -2.5$ is indicated with a dashed line to guide the eye. The results are colour-coded to distinguish the three different ground planes considered.

the correction of the beam chromaticity more difficult and sensitive to electromagnetic property assumptions or measurement errors.

In future works, antenna beam simulations could be improved by collecting more data to model the moisture conditions, leading to a better description of the complex permittivity as a function of depth (Campbell 1990; Bobrov, Repin & Rodionova 2015). Moreover, a more complex frequency dependence with respect to equation (2) could be adopted (for example a Cole–Cole model as in Sternberg & Levitskaya 2001). Note also that the finite accuracy of the numerical solver limits the refinement of the multi-layer model and different EM software solutions should be compared for benchmarking our model.

We followed with computing the beam chromaticity factor and simulated observed beam-averaged sky spectra as a function of frequency and LST, assuming the sky can be described as diffuse synchrotron emission scaled with a constant power law $\beta = -2.5$ across our frequency range. The differences in complex permittivity typical of dry or wet soil conditions translate to a few per cent variations in the beam chromaticty factor with similar amplitude across ground planes, but increasingly more structured in frequency and LST for larger ground planes, as expected.

We modelled the simulated spectra with an N-term log-polynomial exploring N values from 5 to 7, and studied the behaviour of the residuals as a function of N, LST, and beam model, finding negligible frequency structure only for the ideal case of an infinite ground plane.

We added a Gaussian absorption feature to the various simulated spectra to mimic the high redshift 21-cm signal. The final model for the mock measured spectra consisted of the $N^{\rm th}$ term log-polynomial model plus three parameters to describe the Gaussian absorption feature (the central frequency ν_{21}, the amplitude $A_{21,}$ and the width σ_{21}). We studied how beam model uncertainties propagate in the analysis, and bias the Bayesian model parameter reconstruction.

When the exact beam chromaticity correction is applied to the simulated spectra, the model parameters are reconstructed without any bias and residuals are around the mK level. However, we found much larger residuals when the chromaticity is not accounted for, or the beam model for the correction is obtained for different soil conditions or for the different multi-layer implementations. These residuals can reach up to a few hundreds (thousands) of mK for the 10 × 10 m (serrated) ground plane and bias the absorption signal reconstruction. Our results disfavour the use of a large ground plane coupled with the LEDA antenna as it seems that the interaction of the soil and the antenna itself lead to significant oscillating factors on the gain spectral response for all realistic ground plane sizes.

The 3 m × 3 m case behaves better and beam model uncertainties results in smaller parameter bias. Note, however, that a 10 per cent changes in permittivity or conductivity can enhance/reduce the parameters A_{21} and σ_{21} up to a factor of two or shift by few per cent, the recovered central frequency ν_{21}.

Finally, we checked the effect of the various beam models on the reconstructed spectral index β of the simulated spectra and find results in agreement with the input value. We observed a maximum 6 per cent flattening only when the correction for beam chromaticity is not applied.

Apart from some ideal cases, the smooth foreground log-polynomial model is found not to be an accurate description of the frequency structures induced in the observed spectra by realistic LEDA gain patterns, preventing the Bayesian exploration of the parameter space to converge to the expected result. In the future we will investigate how this effect can be mitigated by increasing the number of model parameters used to describe the foreground spatial distribution (e.g. Anstey et al. 2020).

ACKNOWLEDGEMENTS

LEDA research herein was supported in part by NSF grant AST/1616709. MS acknowledges support from the AstroSignals

Synergia grant CRSII5_193826 from the Swiss National Science Foundation. This research made use of `Numpy` (Harris et al. 2020), `Astropy` (The Astropy Collaboration 2013) and `Scipy` (Virtanen et al. 2020). Some of the results in this paper have been derived using the `healpy` (Zonca et al. 2019) and `HealPix` (Górski et al. 2005) package.

DATA AVAILABILITY

The simulated antenna gain patterns used in this work can be found tabulated in `.mat` format in this drive folder.

REFERENCES

Anstey D., de Lera Acedo E., Handley W., 2020, MNRAS, 506, 2041
Anstey D., Cumner J., de Lera Acedo E., Handley W., 2022, MNRAS, 509, 4679
Barkana R., 2018, Nature, 555, 71
Barkana R., Loeb A., 2005, ApJ, 626, 1
Bernardi G., McQuinn M., Greenhill L. J., 2015, ApJ, 799, 90
Bernardi G. et al., 2016, MNRAS, 461, 2847
Bevins H. T. J., Handley W. J., Fialkov A., de Lera Acedo E., Greenhill L. J., Price D. C., 2020, MNRAS, 502, 4405
Bobrov P. P., Repin A. V., Rodionova O. V., 2015, IEEE Transactions on Geoscience and Remote Sensing, 53, 2366
Bowman J. D., Rogers A. E. E., 2010, Nature, 468, 796
Bowman J. D., Rogers A. E. E., Monsalve R. A., Mozdzen T. J., Mahesh N., 2018, Nature, 555, 67
Bradley R. F., Tauscher K., Rapetti D., Burns J. O., 2019, ApJ, 874, 153
Campbell J. E., 1990, Soil Sci. Soc. Am. J., 54, 332
Cohen A., Fialkov A., Barkana R., 2016, MNRAS, 459, L90
Cohen A., Fialkov A., Barkana R., Lotem M., 2017, MNRAS, 472, 1915
Cumner J. et al., 2022, J. Astron. Instrum., 11, 2250001
Danskin W. R., 1998, Technical Report USGS Water-Supply Paper 2370; Chapter H, Evaluation of the Hydrologic System and Selected Water-Management Alternatives in the Owens Valley. United States Geological Survey, California
Davidson D., 2010, Computational Electromagnetics for RF and Microwave Engineering. Cambridge Univ. Press, Cambridge, https://books.google.it/books?id = jDCs1Ckne_EC
Dowell J., 2011, Parametric Model for the LWA-1 Dipole Response as a Function of Frequency
Eastwood M. W. et al., 2018, AJ, 156, 32
Ellingson S. W., Craig J., Dowell J., Taylor G. B., Helmboldt J. F., 2013, in 2013 IEEE International Symposium on Phased Array Systems and Technology, p. 776
Feng C., Holder G., 2018, ApJ, 858, L17
Feroz F., Hobson M. P., 2008, MNRAS, 384, 449
Feroz F., Hobson M. P., Bridges M., 2009, MNRAS, 398, 1601
Fialkov A., Barkana R., 2019, MNRAS, 486, 1763
Fialkov A., Barkana R., Visbal E., Tseliakhovich D., Hirata C. M., 2013, MNRAS, 432, 2909
Fialkov A., Barkana R., Visbal E., 2014, Nature, 506, 197
Field G. B., 1958, Proc. IRE, 46, 240
Furlanetto S. R., Oh S. P., Briggs F. H., 2006, Phys. Rep., 433, 181
Garsden H. et al., 2021, MNRAS, 506, 5802
Gessey-Jones T., Sartorio N. S., Fialkov A., Mirouh G. M., Magg M., de Lera Acedo E., Handley W. J., Barkana R., 2022, preprint (arXiv:2202.02099)
Górski K. M., Hivon E., Banday A. J., Wandelt B. D., Hansen F. K., Reinecke M., Bartelmann M., 2005, ApJ, 622, 759
Harker G. J. A., Pritchard J. R., Burns J. O., Bowman J. D., 2012, MNRAS, 419, 1070
Harris C. R. et al., 2020, Nature, 585, 357
Haslam C. G. T., Salter C. J., Stoffel H., Wilson W. E., 1982, A&AS, 47, 1
Hicks B. C. et al., 2012, PASP, 124, 1090
Hills R., Kulkarni G., Meerburg P. D., Puchwein E., 2018, Nature, 564, E32
Jishnu Nambissan T. et al., 2021, Experimental Astronomy, 51, 193
Liu H., Outmezguine N. J., Redigolo D., Volansky T., 2019, Phys. Rev. D, 100, 123011
Magg M. et al., 2021, MNRAS, 514, 4433
Mahesh N., Bowman J. D., Mozdzen T. J., Rogers A. E. E., Monsalve R. A., Murray S. G., Lewis D., 2021, AJ, 162, 38
Mesinger A., Ferrara A., Spiegel D. S., 2013, MNRAS, 431, 621
Mesinger A., Greig B., Sobacchi E., 2016, MNRAS, 459, 2342
Michalski K., Mosig J., 1997, IEEE Trans. Antennas Propag., 45, 508
Mirocha J., 2014, MNRAS, 443, 1211
Mirocha J., Furlanetto S. R., 2019, MNRAS, 483, 1980
Mirocha J., Harker G. J. A., Burns J. O., 2015, ApJ, 813, 11
Mirocha J., Furlanetto S. R., Sun G., 2017, MNRAS, 464, 1365
Monsalve R. A., Rogers A. E. E., Bowman J. D., Mozdzen T. J., 2017, ApJ, 847, 64
Monsalve R. A. et al., 2020, ApJ, 908, 145
Mozdzen T. J., Bowman J. D., Monsalve R. A., Rogers A. E. E., 2016, MNRAS, 455, 3890
Mozdzen T. J., Mahesh N., Monsalve R. A., Rogers A. E. E., Bowman J. D., 2019, MNRAS, 483, 4411
Muñoz J. B., Loeb A., 2018, Nature, 557, 684
Paravastu H. R. et al., 2007, Impedance Measurements of the Big Blade andFork Antennas on Ground Screensat the LWDA Site
Philip L. et al., 2019, J. Astron. Instrum., 8, 1950004
Presley M. E., Liu A., Parsons A. R., 2015, ApJ, 809, 18
Price D. C. et al., 2018, MNRAS, 478, 4193
Pritchard J. R., Furlanetto S. R., 2007, MNRAS, 376, 1680
Pritchard J., Loeb A., 2010, Nature, 468, 772
Raghunathan A. et al., 2021, IEEE Trans. Antennas Propag., 69, 6209
Reis I., Fialkov A., Barkana R., 2020, MNRAS, 499, 5993
Reis I., Fialkov A., Barkana R., 2021, MNRAS, 506, 5479
Reis I., Barkana R., Fialkov A., 2022, MNRAS, 511, 5265
Sathyanarayana Rao M., Subrahmanyan R., Udaya Shankar N., Chluba J., 2017, AJ, 153, 26
Schmitt H. et al., 2009, Collected LWA Engineering Memos from the Development of the Ground Screen Subsystem
Seyfried M. S., Murdock M. D., 2004, Soil Sci. Soc. Am. J., 68, 394
Seyfried M. S., Grant L. E., Du E., Humes K., 2005, Vadose Zone Journal, 4, 1070
Sims P. H., Pober J. C., 2020, MNRAS, 492, 22
Singh S., Subrahmanyan R., 2019, ApJ, 880, 26
Singh S. et al., 2021, Nat. Astron., 5, 1086
Sokolowski M. et al., 2015, PASA, 32, e004
Spinelli M., Bernardi G., Santos M. G., 2019, MNRAS, 489, 4007
Spinelli M., Bernardi G., Garsden H., Greenhill L. J., Fialkov A., Dowell J., Price D. C., 2021, MNRAS, 505, 1575
Sternberg B. K., Levitskaya T. M., 2001, Radio Sci., 36, 709
Sutinjo A. T. et al., 2015, IEEE Trans. Antennas Propag., 63, 5433
Tallyn E. F., 2002, Technical report, Soil survey of Benton-Owens Valley area, California, parts of Inyo and Mono counties, National Cooperative Soil Survey, Washington, DC
Tauscher K., Rapetti D., Burns J. O., 2020, ApJ, 897, 132
Tauscher K. et al., 2021, ApJ, 915, 66
Taylor G. B. et al., 2012, J. Astron. Instrum., 01, 1250004
The Astropy Collaboration, 2013, A&A, 558, A33
Vedantham H. K., Koopmans L. V. E., de Bruyn A. G., Wijnholds S. J., Ciardi B., Brentjens M. A., 2014, MNRAS, 437, 1056
Virtanen P. et al., 2020, Nat. Methods, 17, 261
Weiner M., 1991, Technical Report, Validation of the Numerical Electro-Magnetics Code (NEC) for Antenna Wire Elements in Proximity to Earth. Mitre Corp Bedford, MA
Wouthuysen S. A., 1952, AJ, 57, 31
Zheng H. et al., 2016, MNRAS, 464, 3486
Zonca A., Singer L., Lenz D., Reinecke M., Rosset C., Hivon E., Gorski K., 2019, J. Open Source Softw., 4, 1298

Zwart J. T. L., Price D., Bernardi G., 2016, HIBAYES: Global 21-cm Bayesian Monte Carlo Model Fitting. preprint (ascl:1606.004)

APPENDIX A: MULTI-LAYER IMPLEMENTATION: CHOICE OF NUMBER OF LAYERS

The multi-layer modelling and its fine-layer implementation, guided by the convergence of the beam gain, have been discussed in Section 2.4 and highlighted in Algorithm 1 and Fig. 2. Some more details on the choice of number of layers are offered here for completeness. Let us denote $\epsilon_{r,i}$ the value of the measurement of relative permittivity at a depth of $|z_i|, i = 1, 2, 3$, while $z_0 = 0$. For the $i + 1$-th sub-layer we have $|z_i| < |z| < |z_{i+1}|$ and the value of ϵ_r at a given z can be obtained through a linear interpolation of the available values:

$$\epsilon_r(z) = \epsilon_{r,i} + \Delta\epsilon_r \frac{|z - z_i|}{|z_{i+1} - z_i|}. \tag{A1}$$

By construction, $\epsilon_r(z) < \epsilon_{r,i+1} = \epsilon_{r,i} + \Delta\epsilon_r$ such that always

$$\lambda_p(z) = \frac{2\pi c_0}{\epsilon_r(z)\nu} > \frac{2\pi c_0}{\epsilon_{r,i+1}\nu} = \lambda_{p,i+1}, \tag{A2}$$

ensuring that the $\lambda_p/10$ rules at the depth $i + 1$-th is stronger than the one for a sub-layer at z. This is important, since we can use the upper integer value $\frac{|z_{i+1}-z_i|}{\lambda_{p,i+1}/10}$ as the number of initial sub-layers beyond the three initial z_i and iteratively double this number until convergence is reached.

APPENDIX B: DEPENDENCE ON THE ASSUMED INPUT ABSORPTION PROFILE

As discussed in Section 3, in this work we focus on the effect of the beam modelling on the analysis using simulated data. We assume for the cosmological signal a simple Gaussian absorption feature with fixed values for the parameters A_{21}, ν_{21}, and σ_{21} (see equation 5). To qualitatively address the consistency of our conclusions with respect to the input 21-cm signal choice, we check in this session the effect varying the parameters of equation (5). We report in Fig. B1, together with the case analysed in the rest of the paper (in magenta in the figure), the reconstructed signal considering i) a similar signal with lower ν_{21} (in green) or ii) an EDGES-type profile (in blue). We focus on our baseline beam model for the 3×3 ground plane. As expected, the results are not identical for the three cases although they all led to conclude that the reconstructed absorption feature is larger, deeper and not necessarily correctly located within the analysed band. We note however that we expect a stronger signal to be less biased. This is why, to be conservative, we have assumed for the analysis in this work an absorption feature shallower than the EDGES results.

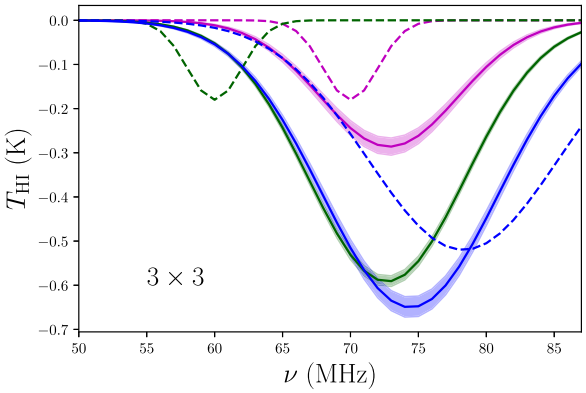

Figure B1. The reconstructed 21-cm absorption profile (solid lines) considering three different input models (dashed lines). The model in blue acts for an EDGES-like type of absorption feature. The simulated spectra are generated considering a 3×3 ground plane and one-layer dry soil conditions and are not corrected for the effect of chromaticity. Shaded area correspond to the propagated 1-σ uncertainties in the parameter posteriors.

APPENDIX C: CHROMATICITY CORRECTION PLOT

We report in this appendix some useful further results to complement the discussions of Section 3.2. We recall that in this work we have explored two main ingredients for the beam simulation: the characteristic of the soil moisture and a multi-layer approach to soil modelling.

We report the percentage difference in the chromaticity pattern between the baseline dry soil condition and ± 10 per cent variation in the input values of permittivity ϵ_r and conductivity σ for the soil in Fig. C1. While the explored variations of the conductivity have a similar impact on the chromaticity correction factors presented in the figure, lowering the permittivity shows an almost inverted pattern for the chromaticity percentage change. Note, however, that the variations are always below 2 per cent.

In Fig. C2, we report instead of the difference in the beam chromaticity between the baseline dry one-layer case and the three or converged multi-layer models described in Section 2.4 (see also Table 2). We explore these differences as a function of the different ground planes used in LEDA analysis.

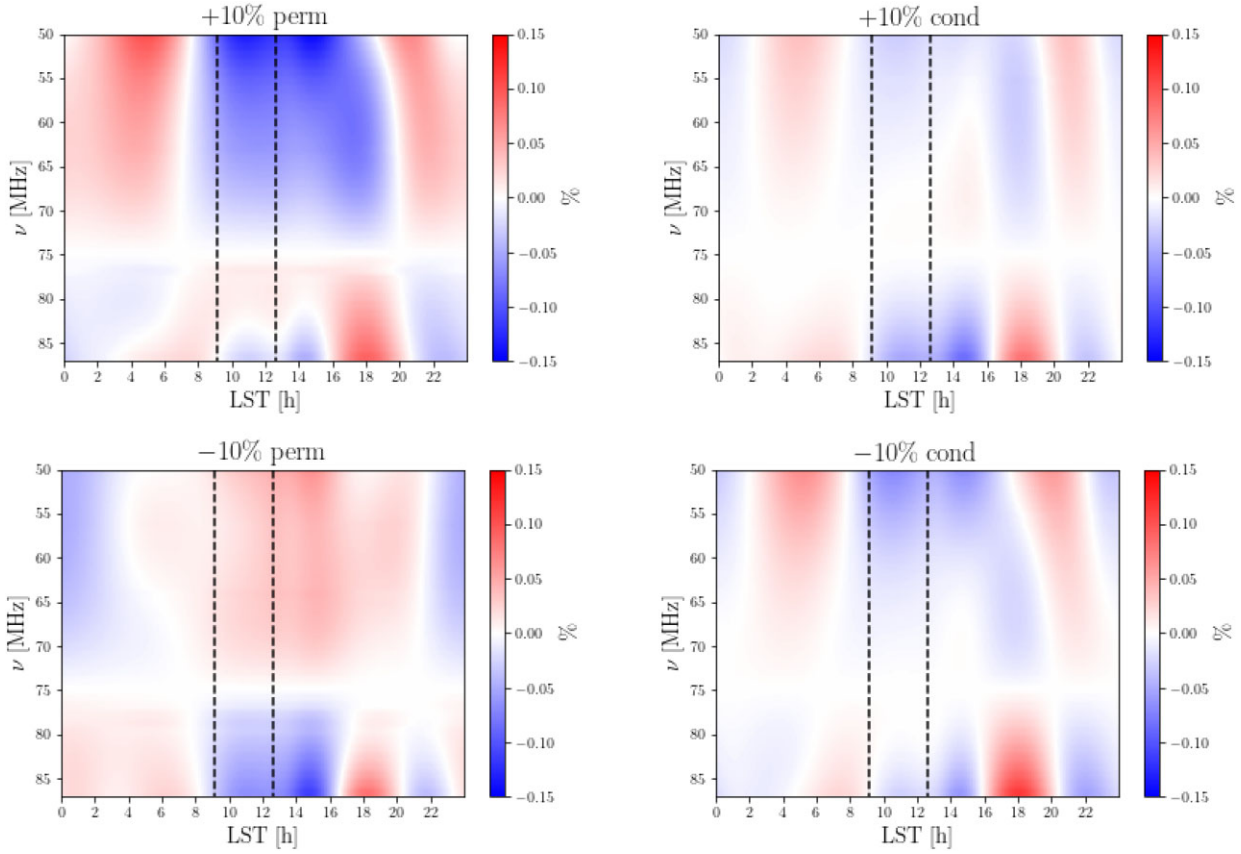

Figure C1. The difference in percentage between the chromaticity factor B_c (see equation 7) computed for the one-layer dry condition FEKO model case and the ones where the or the conductivity are varied by +10 per cent (top row) or by −10 per cent (bottom row). We consider here the 3 × 3 m ground plane.

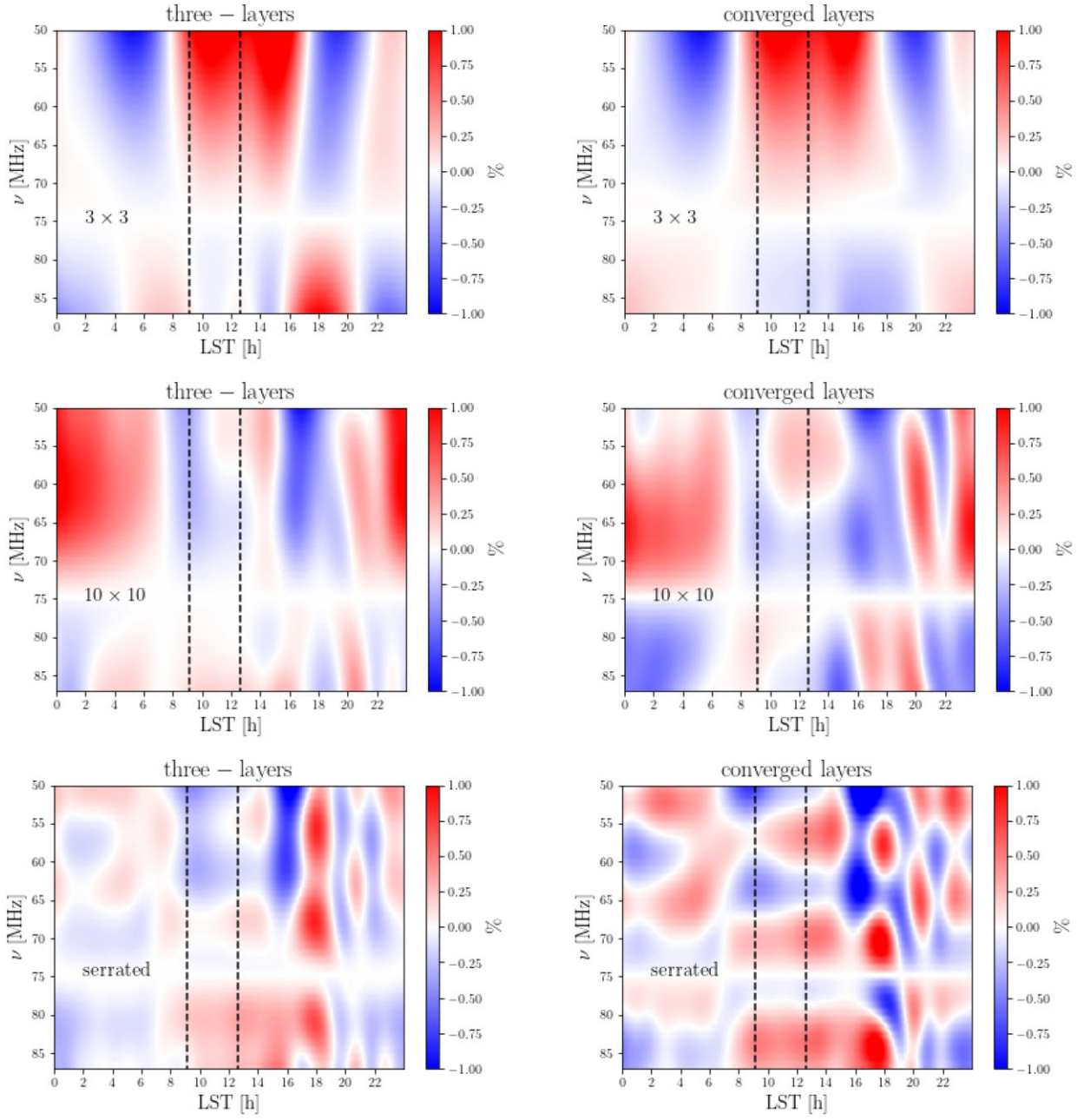

Figure C2. The difference in percentage between the chromaticity factor B_c (see equation 7) computed for the one-layer dry condition FEKO model and the three-layer (left) or the converged layers case (right) for the three different type of ground planes: 3 × 3 (top), 10 × 10 (middle), and serrated (bottom).

APPENDIX D: RESIDUALS WITH RESPECT TO THE SMOOTH FOREGROUND MODEL

As discussed in Section 3.3, assuming no absorption feature, we can assess the impact of a non perfect beam chromaticity correction on the mock sky spectra looking at the residual structure after subtraction of the smooth foreground model of equation (8).

In this appendix, we complement the visual content of Figs 13 and 14 reporting the root mean square (rms) of the residuals in Tables D1 and D2. We recall that we construct the spectra with the baseline model (one-layer, dry soil condition) and then we correct for the effect of chromaticity with a slightly different beam, changing the soil moisture (Table D1) or the soil layering (Table D2), respectively. We analyse different N-term log-polynomial models (5, 6, and 7) and different ground planes (3×3, 10×10, and serrated). Note that the non-corrected and the exact correction cases are the same of in both Tables. Note that best-fitting values for the foreground parameters are obtained with a non-linear least squares solver.

Table D1. The rms (in K) of the residual difference, reported in Fig. 13, between the best-fitting model of equation (8) and the simulated spectra obtained as described in Section 3.1, presented for different polynomial orders ($N = 4, 5, 6$) and for different ground planes. The simulated spectra are obtained considering dry condition and a one-layer description for the soil. The residuals are then computed without any chromaticity correction, with an exact correction using the same beam model as for the spectra in input and for a chromaticity correction computed with wet soil condition instead.

Ground plane	Chromaticity correction	Residual rms (K)		
		$N = 5$	$N = 6$	$N = 7$
3×3	non-corrected	0.086	0.071	0.018
	exact	0.002	0.002	0.002
	wet soil	0.084	0.116	0.019
10×10	non-corrected	0.639	0.942	0.100
	exact	0.002	0.002	0.002
	wet soil	0.226	0.301	0.064
serrated	non-corrected	2.985	3.260	1.279
	exact	0.006	0.006	0.003
	wet soil	2.085	2.491	0.969

Table D2. The rms (in K) of the residual difference, reported in Fig. 14, between the best-fitting model of equation (8) and the simulated spectra obtained as described in Section 3.1, presented for different polynomial orders ($N = 4, 5, 6$) and for different ground planes. The simulated spectra are obtained considering dry condition and a one-layer description for the soil. The residuals are then computed without any chromaticity correction, with an exact correction using the same beam model as for the input spectra, and for chromaticity corrections computed using the three-layer or converged layer model instead.

Ground plane	Chromaticity correction	Residual rms (K)		
		$N = 5$	$N = 6$	$N = 7$
3×3	non-corrected	0.086	0.071	0.018
	exact	0.002	0.002	0.002
	three-layers	0.046	0.031	0.017
	converged layers	0.158	0.151	0.095
10×10	non-corrected	0.639	0.942	0.100
	exact	0.002	0.002	0.002
	three-layers	0.463	0.696	0.154
	converged layers	1.151	1.152	0.268
serrated	non-corrected	2.985	3.260	1.279
	exact	0.006	0.006	0.003
	three-layers	1.661	1.788	1.259
	converged layers	4.802	6.400	4.076

This paper has been typeset from a TEX/LATEX file prepared by the author.